

Systematic error mitigation for the PIXIE Fourier transform spectrometer

A. Kogut^a Dale Fixsen^b Nabila Aghanim^c Jens Chluba^d David T. Chuss^e Jacques Delabrouille^f Brandon S. Hensley^g J. Colin Hill^{h,i} Bruno Maffei^j Anthony R. Pullen^{k,l} Aditya Rotti^d Eric R. Switzer^a Edward J. Wollack^a Ioana Zelko^m

^aNASA Goddard Space Flight Center, 8800 Greenbelt Road, Greenbelt, MD, 20771, USA

^bDepartment of Astronomy, CRESST II, University of Maryland, College Park MD 20740 USA

^cUniversité Paris-Saclay, CNRS, Institut d'Astrophysique Spatiale, Bâtiment 121, 91405 Orsay, France

^dJodrell Bank Centre for Astrophysics, Department of Physics and Astronomy, The University of Manchester, Manchester M13 9PL, UK

^eDepartment of Physics, Villanova University, 800 Lancaster Avenue, Villanova, PA 19085, USA

^fCNRS-UCB International Research Laboratory, Centre Pierre Binétruy, IRL 2007, CPB-IN2P3, Berkeley, CA 94720, USA

^gDepartment of Astrophysical Sciences, Princeton University, Princeton, NJ 08544, USA

^hDepartment of Physics, Columbia University, New York, NY 10027, USA

ⁱCenter for Computational Astrophysics, Flatiron Institute, New York, NY 10010, USA

^jInstitut d'Astrophysique Spatiale, CNRS-Université Paris-Saclay, Orsay, 91405, France

^kCenter for Cosmology and Particle Physics, Department of Physics, New York University, 726 Broadway, New York, NY, 10003, USA

^lCenter for Computational Astrophysics, Flatiron Institute, New York, NY 10010, USA

^mCanadian Institute for Theoretical Astrophysics, University of Toronto, 60 St George Street, Toronto, M5S 3H8, Ontario, Canada

E-mail: Alan.J.Kogut@nasa.gov

Abstract. The Primordial Inflation Explorer (PIXIE) is an Explorer-class mission concept to measure the spectrum and polarization of the cosmic microwave background. Cosmological signals are small compared to the instantaneous instrument noise, requiring strict control of instrumental signals. The instrument design provides multiple levels of null operation, signal modulation, and signal differences, with only few-percent systematic error suppression required at each level. Jackknife tests based on discrete instrument symmetries provide an independent means to identify, model, and remove remaining instrumental signals. We use detailed time-ordered simulations, including realistic performance and tolerance parameters, to evaluate the instrument response to broad classes of systematic errors for both spectral distortions and polarization. The largest systematic errors contribute additional white noise at the few-percent level compared to the dominant photon noise. Coherent instrumental effects which do not integrate down are smaller still, and remain several orders of magnitude below the targeted cosmological signals.

Keywords: CMBR experiments, CMBR polarisation

¹Corresponding author.

1 Introduction

Measurements of the cosmic microwave background (CMB) have played a central role in the development of modern cosmology. The blackbody form of the CMB spectrum provides the foundation for the hot big bang model, tracing the currently-observed expansion of the universe back in time to a hot, dense phase in close thermal equilibrium. Deviations from a perfect blackbody follow the subsequent thermal history as the universe evolves to its present form, providing new tests of the standard cosmological model [1, 2]. Spatial maps of small temperature perturbations about the blackbody mean track density perturbations, providing detailed information on the geometry, constituents, and evolution of the universe [3, 4]. Maps of CMB polarization yield insight into the epoch of reionization, the growth of structure in the low-redshift universe, and offer the tantalizing possibility to detect the signature of an inflationary epoch in the early universe [5–7].

Several decades of instrument development have produced orders-of-magnitude improvement in sensitivity, from the μK sensitivity of the Cosmic Background Explorer [8] to the nK sensitivity proposed for missions in the near future [5–7]. As raw sensitivity improves, careful control of systematic errors are required, as well as means to detect, identify, and correct residual instrumental signatures.

The Primordial Inflation Explorer (PIXIE) is a proposed space mission to measure the frequency spectrum and polarization of the CMB and astrophysical foregrounds on angular scales of 1° and larger [9–11]. Unlike most CMB instruments, which focus incident light onto an array of diffraction-limited detectors each operating within a photometric passband $\Delta\nu/\nu \approx 0.2$, PIXIE interferes two co-pointed beams within a polarizing Fourier Transform Spectrometer (FTS) to measure the autocorrelation function of the sky signal. Although targeting comparable sensitivity as other CMB missions, PIXIE’s different instrumental configuration produces a correspondingly different response to potential systematic errors in both the frequency and spatial domains. Previous papers have described the PIXIE data pipeline and systematic error mitigation for certain classes of instrumental effects [12–14]. In this paper, we extend this treatment to quantify the systematic error mitigation in both the frequency and spatial domains and discuss the power of jackknife tests to identify and remove remaining instrumental signals.

2 PIXIE Instrument and Observations

Figure 1 shows the PIXIE instrument concept. It consists of a polarizing Fourier transform spectrometer with two input ports illuminated by co-pointed beams on the sky. The 55 cm diameter primary mirrors produce circular tophat beams with diameter 2.65° , roughly equivalent to Gaussian beams with 1.65° full width at half maximum. A pair of polarizing wire grids splits the light from each beam into orthogonal linear polarizations then mixes the beams. A movable structure with two mirrors introduces an optical phase delay before a second set of polarizing grids recombines the beams and routes them to the two output ports. Each output port contains a pair of polarization-sensitive bolometers, mounted to absorb mutually orthogonal polarization states.

As the phase-delay mirrors sweep back and forth, each of the 4 detectors samples the resulting interference fringe pattern as a function of the optical phase delay. Let $\vec{E} = E_x\hat{x} + E_y\hat{y}$ represent the electric field incident from the sky. The power P at the detectors as a

function of the phase delay z may be written

$$\begin{aligned}
P_{Lx} &= 1/2 \int \epsilon_{Lx} \{ (f_A E_{Ax}^2 + f_B E_{By}^2) + (f_A E_{Ax}^2 - f_B E_{By}^2) \cos(z\omega/c) \} d\omega \\
P_{Ly} &= 1/2 \int \epsilon_{Ly} \{ (f_A E_{Ay}^2 + f_B E_{Bx}^2) + (f_A E_{Ay}^2 - f_B E_{Bx}^2) \cos(z\omega/c) \} d\omega \\
P_{Rx} &= 1/2 \int \epsilon_{Rx} \{ (f_A E_{Ay}^2 + f_B E_{Bx}^2) + (f_B E_{Bx}^2 - f_A E_{Ay}^2) \cos(z\omega/c) \} d\omega \\
P_{Ry} &= 1/2 \int \epsilon_{Ry} \{ (f_A E_{Ax}^2 + f_B E_{By}^2) + (f_B E_{By}^2 - f_A E_{Ax}^2) \cos(z\omega/c) \} d\omega , \quad (2.1)
\end{aligned}$$

where \hat{x} and \hat{y} refer to orthogonal linear polarizations, ϵ is the (polarized) detector absorption efficiency, f is the transmission through the optics to the detector, L and R refer to the detectors in the left and right concentrators, A and B refer to the two input beams, and ω is the angular frequency of incident radiation. The optical phase delay z is related to the physical mirror position ΔL as

$$z = 4 \cos(\theta) \cos(\delta/2) \Delta L , \quad (2.2)$$

where θ is the angle of incident radiation with respect to the mirror movement, δ is the dispersion in the beam, and the factor of 4 reflects the symmetric folding of the optical path. The factor of 1/2 rather than 1/4 for each of the four detectors results from use of 2 input ports rather than a single port. When both input ports are open to the sky, the power at each detector consists of a dc term proportional to the intensity $E_x^2 + E_y^2$ (Stokes I) plus a term modulated by the phase delay z , proportional to the linear polarization $E_x^2 - E_y^2$ (Stokes Q) in instrument-fixed coordinates. Rotation of the instrument about the beam axis rotates the instrument coordinate system relative to the sky to allow separation of Stokes Q and U parameters on the sky. A full-aperture blackbody calibrator can be deployed to block either of the two input ports, or stowed so that both ports view the sky. With one input

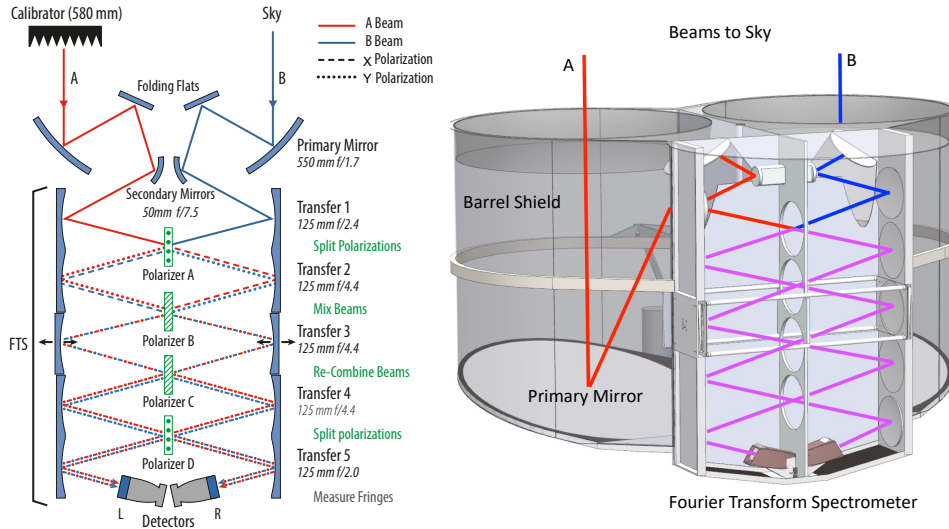


Figure 1. Schematic rendering of the PIXIE instrument, showing the optical path (left) and the beam-forming optics (right). The moving phase-delay mirror pair is highlighted. The Fourier transform spectrometer interferes two co-pointed beams while maintaining all elements within 5 mK of the CMB monopole temperature. The resulting null operation, differential measurement, and complex signal modulation mitigate broad classes of systematic error.

port terminated by the calibrator, the modulated term is then proportional to the difference between the sky signal and the calibrator, providing sensitivity to the sky signal in Stokes I , Q , and U as well as a known reference signal for calibration.

Figure 2 shows the observing strategy. PIXIE will be located at the second Sun-Earth Lagrange point (L2). The spacecraft spins about the instrument boresight while slowly scanning the boresight in a great circle perpendicular to the sun line so that the full sky is mapped every 6 months. For ease of analysis, the mirror stroke, spacecraft spin, and great-circle scan are maintained in a fixed ratio at widely-separated time scales, driven by a single master clock to avoid beat frequencies. The nominal periods of 4 second mirror stroke, 48 second spin, and 18432 second (5.12 hour) scan provide 12 mirror strokes per spin and 384 spins per great-circle scan. Maintaining fixed ratios allows clean separation between the Fourier transforms producing the frequency spectra (mirror stroke), Stokes parameters (spin), and spatial mapping (scan).

The mission data consists of the power on each of the 4 detectors sampled at 256 Hz, supplemented by ancillary data including mirror position, instrument temperatures, and spacecraft pointing. The sampled fringe patterns sorted by mirror position (interferograms, or IFGs) form the basic time-ordered data. The interferograms for each detector are sorted by spin angle and sky pixel, then Fourier transformed with respect to mirror position, spin angle, and sky coordinates to derive frequency spectra for each of the IQU Stokes parameters in each spatial pixel. With HEALPIX pixelization at resolution NSIDE=64 [15], the resulting sky cube has 49152 spatial pixels of diameter 0.9° , each with data from at least 200 independent mirror strokes. Over a 2-year mission, the integration time per pixel ranges from 800 seconds on the ecliptic equator to 50,000 seconds at the north and south ecliptic poles, with a typical mid-latitude pixel observed for 940 seconds.

The frequency resolution within each spatial pixel depends on the mirror stroke and apodization. The nominal mirror stroke length varies to produce either 512 frequency bins of width 19.2 GHz for spectral distortion measurements (calibrator blocking one beam) or 256 bins of width 38.3 GHz for polarization (calibrator stowed) [11]. Scattering filters on the beam-forming optics limit the optical response so that channels at frequencies above ~ 6 THz contain no sky signal.

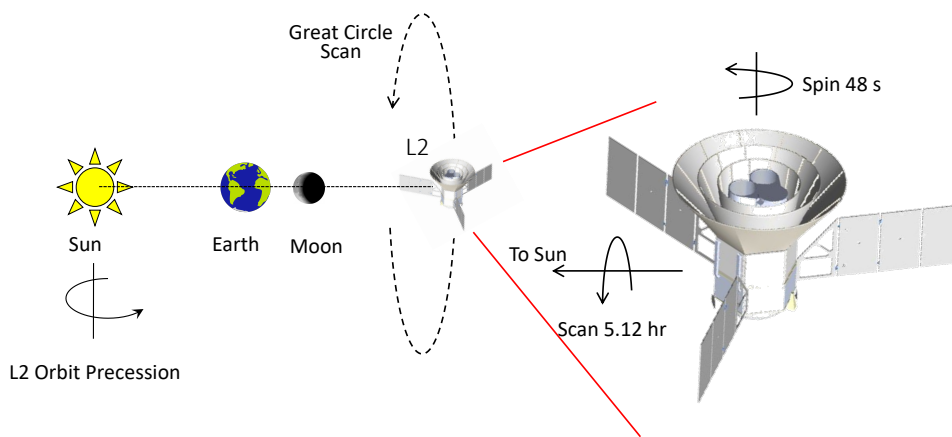


Figure 2. PIXIE will observe at the Sun-Earth L2 point. The spacecraft spins about the beam boresight while simultaneously scanning the beams in a great circle perpendicular to the sun line. The scan pattern maps the full sky every 6 months.

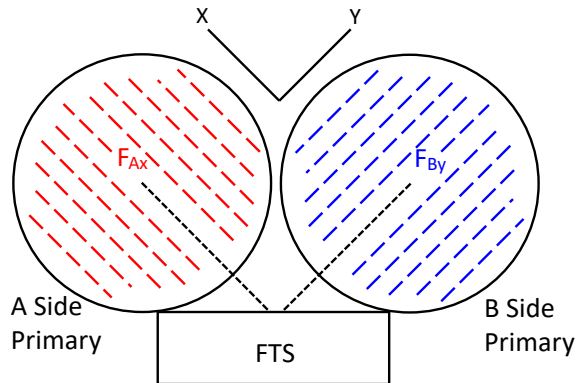


Figure 3. Schematic of the PIXIE optical system viewed from the beam axis, showing the principal instrument symmetry. By construction, the \hat{x} polarization on the A side is simply the mirror reflection of the \hat{y} polarization on the B side.

Comparison of the sky to the blackbody calibrator provide the necessary calibration from digitized telemetry units to surface brightness on the sky [10]. The instrument noise is dominated by photon statistics from CMB monopole and blackbody calibrator, each at 2.725 K. Photon noise from higher-temperature sources (interstellar dust, zodiacal light, and the cosmic infrared background) contributes less than 20% to the total noise for pixels at Galactic latitude $|b| > 20^\circ$.

Instrument symmetry plays a major role in suppressing systematic error. The A and B sides of the instrument are symmetric about the midline between the two primary mirrors (Fig. 3). By construction, the \hat{x} polarization on the A side is simply the mirror reflection of the \hat{y} polarization on the B side. Machining and assembly tolerances break this symmetry and can source systematic error. Section 3 shows how the instrument symmetry and Fourier transform minimize potential systematic error, while Section 4 discusses jackknife tests to identify and correct residual errors.

3 Systematic Error

Systematic errors may be defined as non-random effects from the instrument and data processing which create organized differences between the true sky and its representation in data. An extensive literature discusses common sources of systematic error and mitigation strategies for CMB measurements [12–14, 16–24]. A useful taxonomy distinguishes between additive effects (which exist independent of specific sky signals) and multiplicative effects (which modulate sky signals but vanish if the underlying sky signal is not present). Examples of the former include post-detection electronics pickup, instrumental emission, and $1/f$ noise, while the latter includes effects such as gain error, bandpass error, and beam effects.

Several strategies have proven effective for the suppression, mitigation, and identification of systematic error. Null operation maintains the instrument near the same temperature as the sky, minimizing offsets generated by internal absorption, emission, or reflection. Differential operation compares signals to cancel common-mode emission from unwanted sources while reducing the effect of post-detection gain fluctuations. Signal modulation imposes a pre-determined time-ordered variation on specific input signals; subsequent matched demod-

ulation separates the desired signals from other (unmodulated) sources. Jackknife tests – the comparison of equivalent data sets sorted by some external factor – provide a blind method to search for residuals down to the level of the noise in the selected data. While PIXIE employs all of these methods, we focus below the role of the FTS in systematic error suppression.

3.1 Additive Effects

Additive effects are independent of the sky signal. We review common additive effects and use simulations to assess their impact on the PIXIE data.

3.1.1 Additive Periodic Signals

Signals that repeat with a fixed period commensurate with the sky scan can build up to observable levels. Common examples are electronic pickup of signals at harmonics of the beam motion across the sky or (for polarization) harmonics of the spin period or other polarization modulation. We use noiseless simulations to assess the extent to which the FTS can suppress such signals. We generate 6 months of time-ordered data for a single detector, consisting of a sine wave of unit amplitude and fixed period, and tag each time-ordered sample with the FTS phase delay, spin angle, and sky pixel. We then project the time-ordered data into sky pixels using the HEALPIX pixelization at resolution NSIDE=64. With no FTS, the simplest mapping scheme bins the data from a single detector by spin angle and sky pixel to project the sine signal into full-sky maps in Stokes IQU parameters. Including the FTS, we sort the time-ordered data for a single detector into individual interferograms, perform the Fourier transform to the frequency domain, and sort the synthesized spectra by spin angle and sky pixel to derive the IQU parameters in each voxel.

Figure 4 shows the resulting IQU maps for sinusoidal modulation at twice the spin frequency. As expected, sorting the signal by sky pixel and spin angle simply projects the spin-modulated signal into the Q and U polarization maps at unit amplitude. After Fourier transform, the Q and U maps show a similar spatial striping pattern, but with amplitude reduced by a factor of 30 in the lowest synthesized frequency channel and falling as $\nu^{-5/2}$ in higher frequency channels.

3.1.2 Internal Emission and Reflection

Emission and reflection within the instrument can induce additive systematic error, both from elements directly in the optical path from the detectors to the sky (mirrors, grids) as well as any stray-light view from the detectors to the walls of the instrument. To minimize these effects, the entire optical path – primary mirrors, secondary mirrors, folding flat, FTS, and all surrounding walls – is maintained at temperatures within a few mK of the 2.725 K CMB monopole. The largest possible instrumental signal is thus determined by the few mK maximum temperature difference between the instrument and the sky. Isothermal operation alone reduces systematic errors from internal absorption or reflection by a factor of 250 compared to instruments with 4 K optics, and a factor of 50,000 compared to room-temperature optics.

The double-differential design provides additional mitigation. By Kirchoff’s law, sky photons absorbed by the mirrors or grids are replaced by emitted photons whose spectrum is well approximated as a modified blackbody at the instrument temperature,

$$I_\nu = \kappa \left(\frac{\nu}{\nu_0} \right)^\alpha B_\nu(T_{\text{inst}}) . \quad (3.1)$$

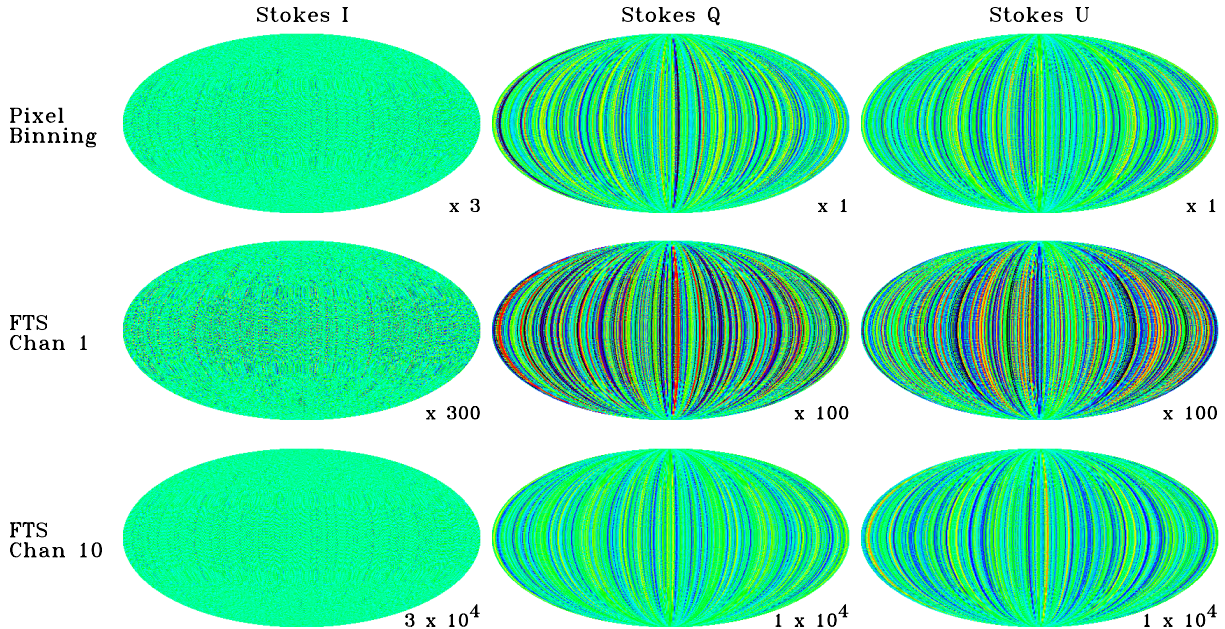


Figure 4. Sky maps generated from an additive sinusoidal signal of unit amplitude at twice the spin frequency are shown for the PIXIE scan pattern (Mollweide projection in ecliptic coordinates). Compared to simple pixel binning, the FTS suppresses the projection into Stokes Q and U with a steep frequency dependence. Maps have been scaled in amplitude as noted to allow a common color stretch.

For clean aluminum surfaces, $\alpha = 1/2$ with $\kappa = 0.002$ at reference frequency $\nu_0 = 100$ GHz [25], so that the error signal from any single surface is of order $10^{-5} \partial B_\nu / \partial T$ where $\partial B_\nu / \partial T$ is the temperature derivative of a blackbody spectrum at $T = 2.725$ K. The FTS then differences the signal from each optical surface on the A side of the instrument against the comparable signal from the corresponding surface on the B side. After Fourier transform, the resulting systematic error signal is proportional to the double difference of the component emissivities and temperatures,

$$I_\nu = \Delta\kappa \times \frac{\partial B_\nu}{\partial T} \times \Delta T_{\text{inst}} . \quad (3.2)$$

With $\Delta\kappa < 0.01 \kappa$ and $\Delta T_{\text{inst}} < 5$ mK, the maximum error in the time-ordered data is now of order $10^{-7} \partial B_\nu / \partial T$ [12].

Mission operations further mitigate the impact of differential emission. If the temperature difference between optical components on the A and B sides were constant in time, the error signal (Eq. 3.2) would have peak amplitude of 100 Jy sr^{-1} , comparable to the cosmological signals. Throughout the mission, the temperature of each optical component is individually controlled to $100 \mu\text{K}$ accuracy and $1 \mu\text{K}$ knowledge. Twice each great-circle scan (as the beams cross the north and south ecliptic poles) all component temperatures are set to new values such that the time-ordered temperature profile of any component is orthogonal with any other component. It is easily arranged to spend half the mission with positive temperature difference $+\Delta T_{\text{inst}}$ between corresponding optical surfaces and half with negative difference $-\Delta T_{\text{inst}}$. The systematic error thus cancels in the signal mean, contributing only

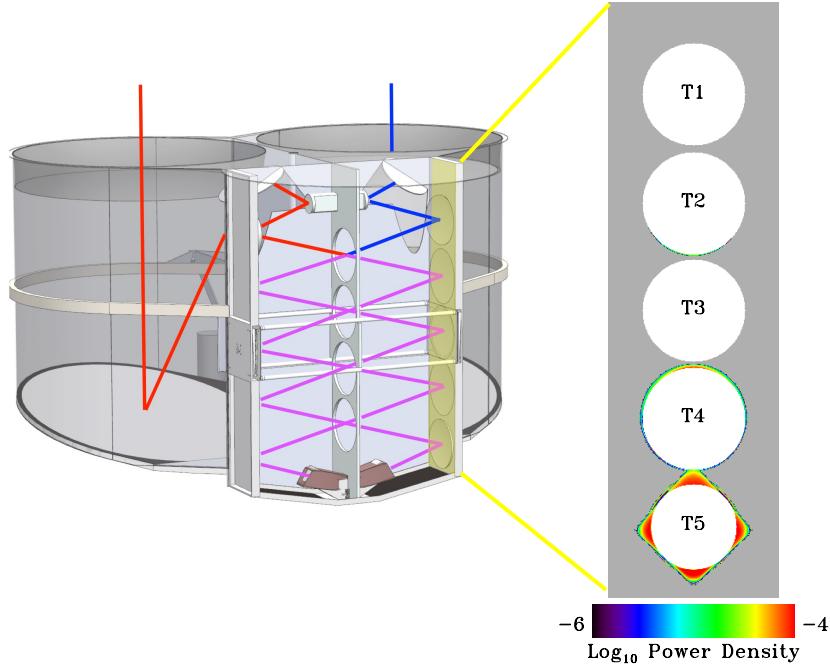


Figure 5. Stray-light illumination pattern on the instrument wall surrounding the FTS transfer mirrors. Emission from components below the MTM (e.g. spillover at mirrors T4 and T5) is not modulated by the FTS phase delay. Temperatures of the mirrors, polarizers, and walls are under active thermal control and periodically varied to separate stray light from sky signals.

to the variance¹. More generally, we extend the sky map software [14] to include nuisance terms

$$\kappa_i T_{\text{inst},i}(t) \quad (3.3)$$

proportional to the temperature of each optical component, effectively measuring the coupling to each optical surface. After marginalization over the nuisance parameters, the residual depends on the integrated noise δT_{therm} in the thermometer readout for each component,

$$\delta I_\nu = \Delta\kappa \times \frac{\partial B_\nu}{\partial T} \times \delta T_{\text{therm}} . \quad (3.4)$$

The thermometers are read out once per second with read noise $1 \mu\text{K}$. Over the course of a 2-year mission, the read noise for each component integrates down to precision $\delta T_{\text{therm}} \approx 0.1 \text{ nK}$, resulting in residual error $\delta I_\nu < 10^{-5} \text{ Jy sr}^{-1}$. Since T_{inst} varies symmetrically about the sky temperature, the nuisance signal is nearly orthogonal to the sky signal. The addition of ~ 20 global nuisance parameters thus increases the noise in the fitted sky cubes by a negligible amount. Note that the correction only requires knowledge of the temperature change in each component; absolute thermometry is not required.

Emission from the instrument walls can scatter into the beams to reach the detectors. We model the resulting stray-light signal using a ray-trace code in the geometric optics limit. For each linear polarization, we generate a set of 10^9 outgoing (skyward) rays, each originating from a random position on the detector and with a random skyward direction. A

¹By appropriate choice of weights in the time domain, the cancellation can be made nearly exact.

ray-tracing algorithm follows each ray through the optical path. Rays that miss the active optical elements terminate on the walls of the instrument, which are coated with a microwave absorber. Figure 5 shows the density of stray-light rays terminating on the wall containing the transfer mirrors within the FTS. A circular cold stop at the 0.1 K horn mouth acts as a pinhole camera to re-image the square base of the horn onto the FTS exit port (mirror T5). 12% of the rays exiting the concentrator terminate on the wall surrounding mirror T5, with an additional 2% terminating at mirror T4. Since these rays do not undergo the FTS phase delay, they do not generate a fringe pattern and instead only appear as part of the unmodulated term in Eq. 2.1. As with the mirrors, each wall is under active thermal control and maintained within a few mK of the sky temperature. Un-modulated stray light may thus be treated as an additive systematic error signal with maximum amplitude of 0.01% of the total power (dominated by the CMB monopole). Since the time constants for individual temperature-controlled components (~ 10 seconds) are slow compared to the 4-second mirror sweep, component temperatures cannot vary rapidly compared to individual interferograms. The resulting stray-light signal from the wall surrounding Transfer Mirror 5 produces a systematic error $< 10^{-3}$ Jy sr $^{-1}$.

Stray light originating from components skyward of Polarizer B undergo beam-splitting and phase delay and produce fringes at the detector. The ray-trace analysis shows that 0.3% of the beams terminate on these surfaces, primarily around Transfer Mirror 2. Since the walls are within a few mK of the sky temperature, the un-corrected error signal after Fourier transform is thus of order

$$I_\nu = 0.003 \times \frac{\partial B_\nu}{\partial T} \times \delta T_{\text{inst}} \quad (3.5)$$

or 10^3 Jy sr $^{-1}$. As with the active optical elements, the skymap software includes nuisance terms proportional to the variation in wall temperature (*cf* Eq. 3.3) to separate emission originating within the instrument from true sky signals. After correction, all stray-light terms contribute $\delta I_\nu < 10^{-3}$ Jy sr $^{-1}$.

Internal reflections can also contribute a systematic error signal. The instrument calibration and subsequent sensitivity to CMB spectral distortions depends on in-flight observations of a full-aperture blackbody calibrator. The calibrator consists of an array of absorbing cones mounted on an thermally-conductive aluminum backplate, with power reflection coefficient at normal incidence $R < -65$ dB [10]. The cone tip heights are staggered and the entire calibrator is tipped by 2° to mitigate standing waves within the instrument. Rays originating from the detector and reflecting from the calibrator terminate elsewhere within the instrument. Since the instrument and calibrator are maintained within a few mK of each other, the uncorrected error signal

$$I_\nu = 10^{-6.5} \times \frac{\partial B_\nu}{\partial T} \times \delta T_{\text{inst}} \quad (3.6)$$

is below 1 Jy sr $^{-1}$. Since the reflected rays terminate on components under active thermal control, reflections are accounted for in the above-described nuisance parameters.

3.1.3 Cosmic Rays

Galactic cosmic-ray protons in the energy range 0.1–1 GeV can impact the detector assembly to deposit energy uncorrelated with the sky signal, creating an additional additive systematic effect. Two effects dominate. Energy deposited in the detector frame creates a stochastic background of thermal fluctuations, sourcing corresponding fluctuations in the bolometer

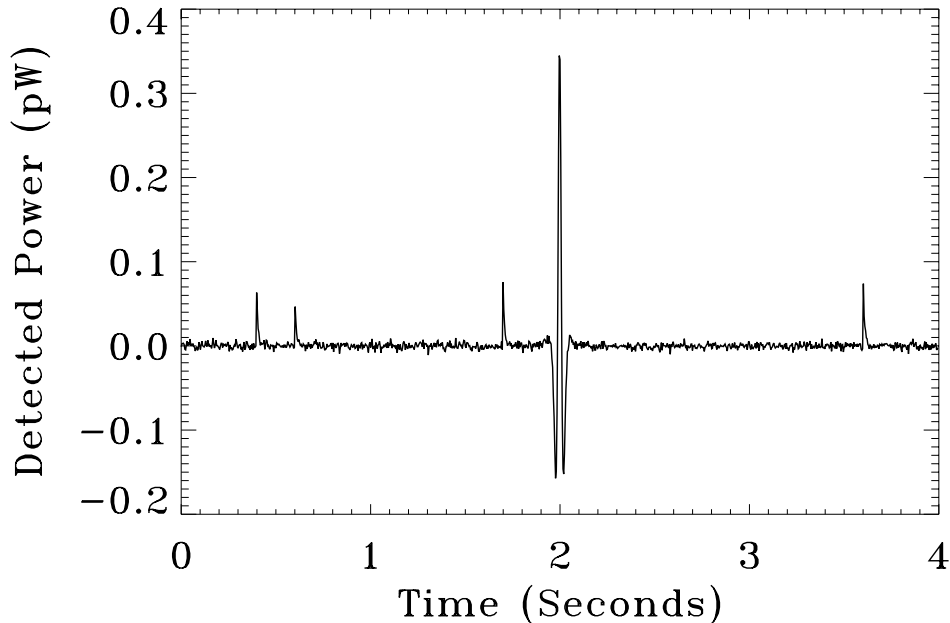


Figure 6. Simulated interferogram including sky signals, instrument noise, and random cosmic-ray hits. Individual cosmic-ray hits to the detector absorber are observed at high signal-to-noise ratio and are co-added to create a template for cleaning.

output signal. This effect, common to all bolometric detectors, can be mitigated by tightly coupling the detector frame to a well-controlled thermal bath. PIXIE’s single-crystal-silicon detector frames include a 4 mm^2 pad of $4 \text{ }\mu\text{m}$ thick electroplated gold (residual resistivity ratio $\text{RRR} > 50$) on each corner of the frame. Gold wires bonded to each pad facilitate heat transport from the frame to the bath, following the design from the Hitomi Soft X-ray Spectrometer microcalorimeters [26]. The predicted thermal fluctuations for PIXIE from cosmic ray hits to the detector frame is $0.01 \text{ }\mu\text{K Hz}^{-1/2}$, a factor of 30 below the thermal noise from the adiabatic demagnetization refrigerator.

Cosmic ray hits directly on the bolometer absorbing structure cannot be reduced by additional heat sinking, but must be dealt with in the data processing pipeline. Figure 6 shows a simulation of cosmic-ray hits to a single interferogram. The Planck mission, operating near solar minimum with correspondingly high rates of Galactic cosmic ray events, saw hit rates of order $1\text{--}2 \text{ min}^{-1}$ directly to the spider-web absorber [27]. The PIXIE absorber grid is larger ($12.7 \times 12.7 \text{ mm}$ with 11% fill factor), leading to an estimated hit rate of $1\text{--}2$ hits per second. A typical cosmic ray hit deposits 1.8 keV of energy within the $1.4 \text{ }\mu\text{m}$ thick silicon grid. The signal-to-noise ratio is thus $15\text{--}20$ at the peak of a single event, increasing to 40 when integrated over the subsequent thermal decay. A 2-year mission provides 8×10^6 cosmic ray hits to be co-added for each detector (5% of the total time-ordered data samples), providing an excellent basis for an empirical model of the resulting thermal decay.

As with Planck, individual cosmic ray events will be flagged and co-added to produce a model for cleaning the time-ordered data. Figure 7 compares the effect of cosmic ray hits before and after cleaning. We generate noiseless simulations of time-ordered cosmic-ray events for a full two-year mission, Fourier transform each interferogram to generate frequency spectra, and sort the spectra by spin angle and sky pixel to produce IQU data cubes. If

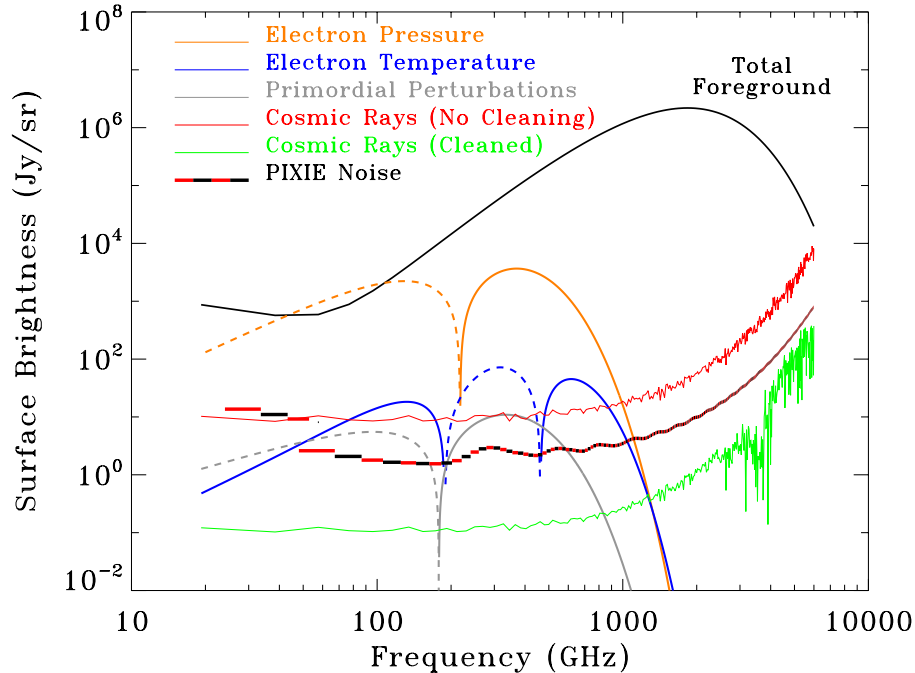


Figure 7. Synthesized frequency spectra generated from a noiseless simulation of cosmic-ray events over a 2-year mission are compared to the instrument noise and unpolarized sky signals. Dashed lines show negative signals. Cleaning the individual cosmic-ray events with 1% accuracy reduces the residual to negligible levels.

nothing were done to identify or clean cosmic-ray hits, the resulting cosmic-ray noise in the frequency domain would lie a factor of ten above the instrument noise². Cleaning the data reduces the residual amplitude of individual cosmic-ray events and modifies the time-ordered structure, replacing the original sharp peak and subsequent decaying exponential with a smaller and smoother residual. Here we model the residual as a damped sinusoid with period twice the thermal time constant of the absorber, and adjust the amplitude to show a residual with 1% of the power in the un-cleaned signal. Cleaning at this level reduces the cosmic-ray noise to negligible levels.

3.1.4 Correlated Noise

Noise with non-zero correlation in the time domain – often called $1/f$ noise for its frequency dependence – is a common source of additive systematic error. Figure 8 shows an example. Depending on the scan strategy, correlations between successive samples lead to pixel-to-pixel correlation (striping) in the map domain.

Figure 9 shows 6-month sky maps generated from a random noise simulation consisting of $1/f$ noise with knee frequency 0.1 Hz. As in §3.1.1, we compare sky maps for simple pixel binning (without the FTS) to the spatial/frequency sky cubes produced by the FTS.

²Both the instrument noise and cosmic-ray spectra are nearly independent of frequency. The rise in noise amplitude at frequencies above 1 THz results from referring the detected noise to the sky signal, which is attenuated at high frequencies by a set of low-pass filters.

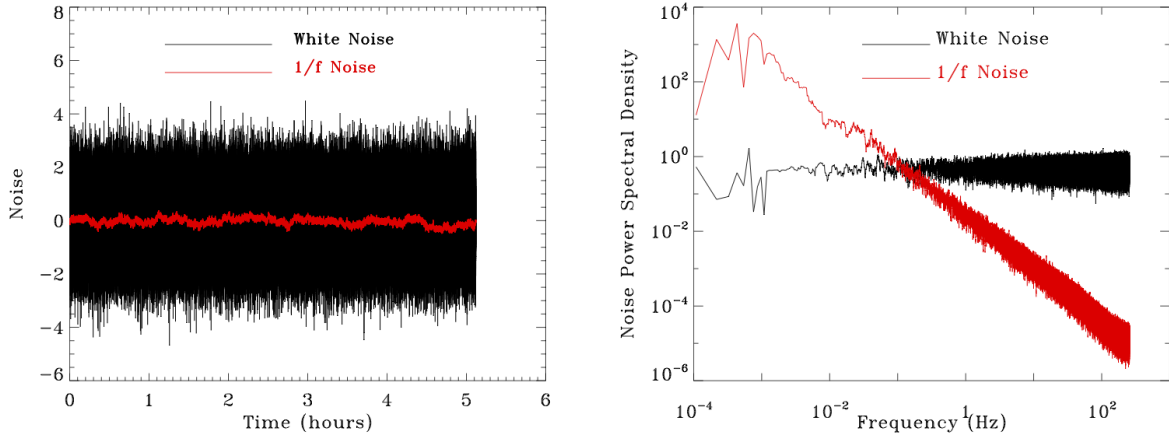


Figure 8. Time ordered data (left) and power spectral density (right) are shown for simulated white and $1/f$ noise components over a single great-circle scan. The $1/f$ knee frequency of 0.1 Hz is fast compared to the 48 seconds required for the instrument boresight to sweep across a single pixel, but slow compared to the 4-second FTS phase delay stroke.

The spatial striping is evident for pixel binning, both for Stokes I and in polarization. The PIXIE Fourier transform effectively whitens $1/f$ noise. Figure 10 compares the angular power spectra for the white noise and $1/f$ components within the two mapping schemes. The white-noise component appears at comparable amplitudes regardless of the mapping

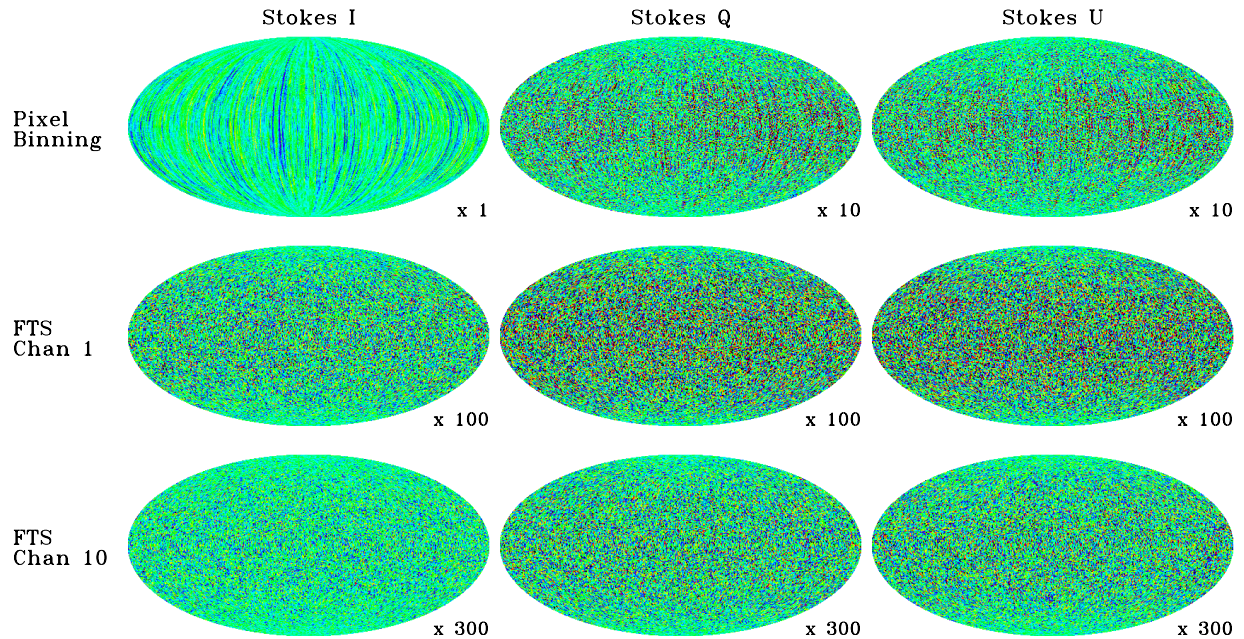


Figure 9. Sky maps generated from simulated $1/f$ noise are shown for the PIXIE scan pattern (Mollweide projection in ecliptic coordinates). Simply binning the time-ordered data by sky pixel leads to striping in the maps, while the FTS effectively whitens the $1/f$ component. Maps have been scaled in amplitude as noted to allow a common color stretch.

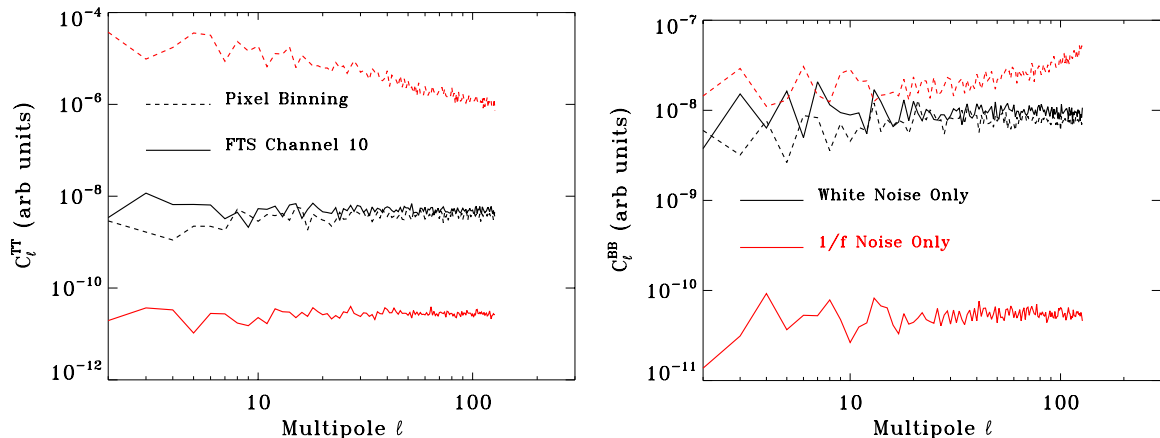


Figure 10. Angular power spectra for the maps shown in Figure 9 for both white noise (black) and $1/f$ noise with knee frequency 0.1 Hz (red). The usual $\ell(\ell+1)/(2\pi)$ normalization has been suppressed so that white noise shows as a horizontal line. While the white-noise amplitudes are comparable for both the pixel binning (dashed lines) and FTS maps (solid lines), the FTS whitens and suppresses the $1/f$ component.

scheme, but the FTS provides orders-of-magnitude suppression for the $1/f$ component in both the polarized (BB) and unpolarized (TT) power spectra as compared to simple pixel binning. The FTS samples the $1/f$ noise at frequencies between the 256 Hz detector sampling and the 0.25 Hz mirror stroke. The constant-velocity FTS mirror stroke produces a linear relation between the frequencies at which the data are sampled and the optical frequencies after Fourier transform, $\nu_{\text{data}} = v/c \nu_{\text{opt}}$ where $v = 4 \text{ mm s}^{-1}$ is the phase velocity of the mirror stroke. The projected $1/f$ noise is thus largest in the lowest synthesized frequency channel and decays as ν^{-1} for higher channels.

3.2 Multiplicative Effects

Multiplicative effects modulate the input signal difference. The differential design and operation near null reduce the amplitude of such effects, but do not entirely eliminate them. End-to-end simulations evaluate the response in the PIXIE data.

3.2.1 Calibration Error

The instrument calibration converts the signal at the detector from digitized telemetry units to physical units of surface brightness. Time-dependent variation in the calibration, if not corrected in the analysis, can propagate through the Fourier transform to produce systematic errors in the resulting sky spectra.

Instrument calibration compares data taken during two consecutive great-circle scans, one with the calibrator blocking the A-side beam and the second with the calibrator blocking the B-side beam. Since input signals change sign when observed in the A beam vs the B beam (Eq. 2.1), the sky signal in each map pixel cancels when summing the scan data for that pixel, leaving only the difference in the calibrator signal. The differential calibrator signal averaged over the scan circle provides an absolute blackbody reference for signal calibration. A 5 mK temperature change in the external calibrator produces a signal difference 3–5 orders of magnitude above the instrument noise or thermometry uncertainty (Figure 11), allowing

determination of the instrument calibration to a few parts in 10^6 every 10 hours throughout the mission [10].

Calibration errors at this level produce negligible artifacts in the sky spectra. After calibration, the data for a single detector may be written as

$$P_{Lx,cal} = [G_0(t) + \delta G(t)] [\int \{ (E_{Ax}^2 + E_{By}^2) + (E_{Ax}^2 - E_{By}^2) \cos(z\omega/c) \} d\omega] \quad (3.7)$$

where $G_0(t)$ is the true calibration (which may vary in time) and $\delta G(t)$ represents the error. The constant term $E_x^2 + E_y^2$ is dominated by the CMB monopole which does not vary across the sky. Gain errors $\delta G(t) \times (E_x^2 + E_y^2)$ in this term are thus equivalent to additive systematic errors discussed above. With $\delta G/G \lesssim 10^{-6}$, the resulting error signal has amplitude of a few μK in the time domain prior to mapping, and less than 1 nK after mapping (*cf* §3.1.1) and §3.1.4.

Gain errors in the Fourier transform are similarly small. Fluctuations in the post-detection electronics can produce $1/f$ variation in the calibration as well as variation locked to specific instrument time scales (e.g. spin). Figure 12 shows an example of $1/f$ gain error. We first generate the ideal interferogram $P(z)$ as a function of mirror position z which would be produced by a typical unpolarized sky signal, including median foreground contributions as well as the $30 \mu\text{K}$ CMB anisotropy. We then generate a $1/f$ time series $\delta G(t)$ with rms amplitude 10^{-5} and 1 mHz knee frequency for a single 10-hour calibration period to produce the time-ordered error signal

$$\delta P = \frac{\delta G(t)}{G_0} P(z(t)) \quad (3.8)$$

in successive interferograms. The Fourier transform of each successive interferogram produces a series of sky spectra, which we co-add to derive the mean error in the calibrated sky spectra. Note that mirror reverses direction after every stroke, effectively negating the contribution from gain drifts on time scales longer than the mirror stroke. As expected, the effect of slow

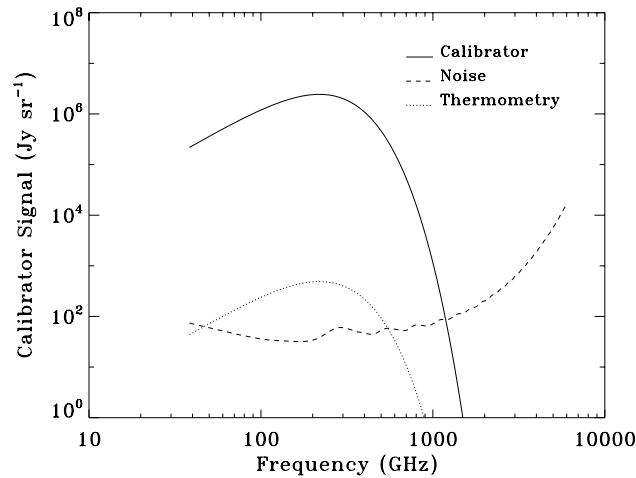


Figure 11. The calibration signal from a 5 mK temperature change in the external calibrator is large compared to instrument noise during the measurement or the $1 \mu\text{K}$ differential thermometry precision. Calibration drifts can be tracked to few-part-per-million precision on time scales of a few hours or longer.

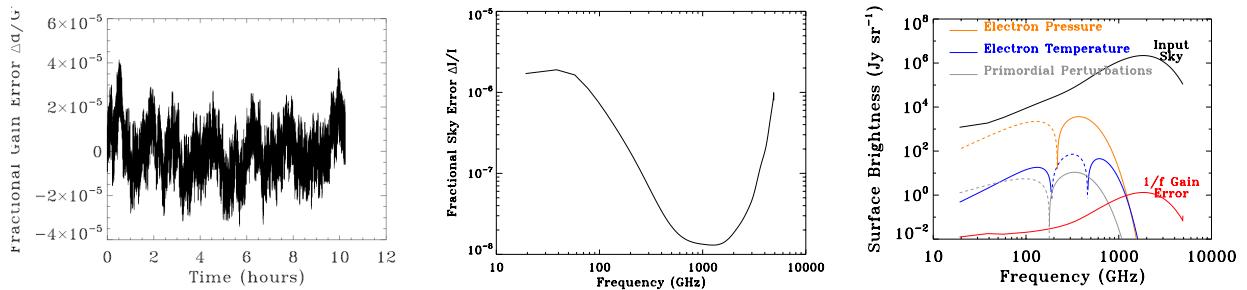


Figure 12. (Left) Simulated $1/f$ gain variation with 1 mHz knee frequency. (Center) Fractional error in the recovered sky spectrum resulting from $1/f$ gain drift. (Right) The systematic error in the recovered sky spectrum is small compared to the cosmological signals.

gain drifts is most pronounced in the first few synthesized frequency channels. A fractional gain error $\delta G(t)/G = 10^{-5}$ produces a comparable fractional error $\Delta I/I$ in the first few channels of the sky spectra, and falls rapidly for higher frequency channels. The resulting error ΔI_ν in the sky spectra is below 1 Jy sr^{-1} at all frequencies and is negligible compared to the instrument noise or cosmological signals.

Gain modulation at harmonics of the spin period can be sourced by corresponding variation in the instrument temperature or power system. The 48-second spin period with axis perpendicular to the sun line produces a “barbecue roll” illumination of the observatory exterior surface (Figure 2). The 75-second barbecue roll for the Cosmic Background Explorer produced synchronous variation in the instrument electronics temperature below 10 mK [16]. Electronics components typically show thermal gain variation at levels of a few percent per K. The faster PIXIE spin would thus be expected to produce spin-locked gain variation at levels $\delta G/G \approx 10^{-4}$ or less. As with $1/f$ gain modulation, the primary effect of spin-locked modulation is on the detector total power, generating spatial striping similar to the additive signals in Figure 4. Figure 13 shows the rms amplitude of the spin-locked signals for selected harmonics of the spin period. Gain modulation of the detector total power produces negligible artifacts in either total intensity or polarization. Variation in the detected power as a function of mirror position is less than 1% of the total power: spin-locked gain modulation of the interferogram produced by anisotropic sky signals is even smaller.

Errors in the calibrator thermometry can also source systematic errors. Each of the thermometers within the external calibrator are read out once per second with read noise $1 \mu\text{K}$, which integrates down to few-nK precision during a single 10-hour calibration cycle. The absolute thermometry scale is set in flight to accuracy $10 \mu\text{K}$ using observations of Galactic emission lines and the Wien displacement law for the measured blackbody spectra [10, 17]. Since the sky spectra are referred to the blackbody calibrator, errors in the absolute thermometry affect the calculated monopole temperature T_0 but cancel to first order for spectral distortions, resulting in systematic error $\delta I_\nu < 5 \times 10^{-3} \text{ Jy sr}^{-1}$ for the derived spectral distortions.

3.2.2 Bandpass Error

Comparison of signals between different detectors can lead to systematic error if different detectors have different frequency response. Sharp spectral features such as line emission are particularly problematic. Measurements of polarization by the Planck mission required

careful correction for the differential bandpass of individual detectors [28–30]. PIXIE does not use bandpass filters to define individual spectral channels, but instead relies on Fourier transform of the measured interferograms to derive the spectra within synthesized frequency channels. An ideal FTS allows a single detector to produce data at a large number of well-characterized frequency channels, with the channel width (and hence channel center frequencies) determined by the maximum mirror throw, the number of channels (and hence the highest synthesized frequency) set by the number of detector samples within an interferogram, and the channel-to-channel covariance determined by the interferogram apodization [10]. For convenience, the PIXIE channel widths are commensurate with the CO J=1-0 line at 115.3 GHz, $\Delta\nu = \nu_{\text{CO}}/N$ so that every N^{th} channel is centered on a CO line. The total optical passband is limited by scattering filters on the beam-forming optics. Both the scattering filters and the mirror sampling are common to all four detectors. Frequency dependence in the individual detector absorption coefficients or the optical transmission from the detector to the sky can be identified and characterized by detector-to-detector comparison of the blackbody calibrator (§4.5).

3.2.3 Beam Errors

An extensive literature discusses potential systematic error and mitigation strategies related to beam shape [19, 21, 31, 32]. This is of particular concern for polarization measurements, which commonly rely on differencing the signal between two beams on the sky. Differential beam shape can then produce leakage between polarization and the much brighter unpolarized signals.

PIXIE’s differential design and mission operations mitigate beam errors. Each detector is intrinsically sensitive to the difference in polarization seen by two co-pointed beams (Eq.

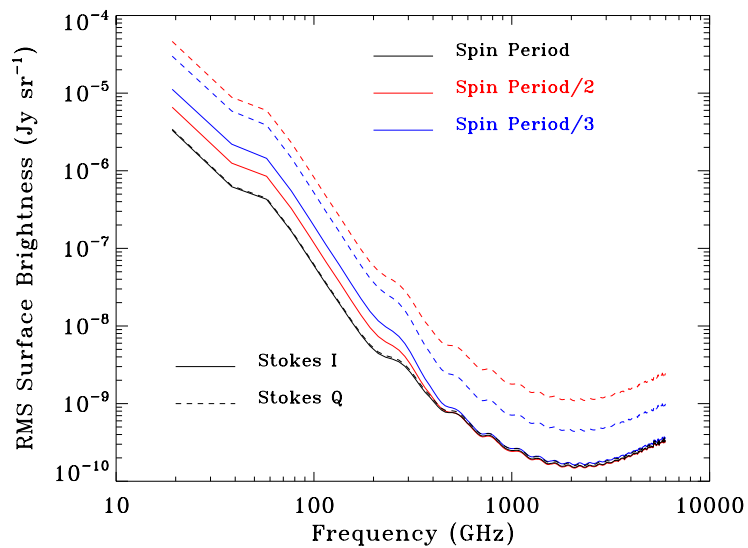


Figure 13. Thermal variation of the instrument electronics can modulate the post-detection gain to create striping in the maps. The figure shows the RMS amplitude of the striping for gain modulation with amplitude $\delta G/G = 10^{-4}$ at selected harmonics of the spin period. Solid lines show the spectra for unpolarized emission (Stokes I) while dashed lines show the spectra for Stokes Q.

2.1) so that systematic errors coupling unpolarized temperature gradients to a false polarized signal cancel to first order for any individual detector and to second order when comparing detectors [13]. The instrument is symmetric about the midline between the two beams (Fig. 3), so that the \hat{x} polarization from one beam is the mirror reflection of the \hat{y} polarization from the other beam. Temperature-polarization mixing thus depends on anti-symmetric component of the difference between the A and B beams on the sky.

PIXIE’s multi-moded light-bucket optics produce a circular tophat beam for each detector. Since there is only one spatial pixel, centered on the optical axis, beam effects such as coma and aberration are minimized. In this, PIXIE differs from most CMB imaging instruments, which employ kilo-pixel arrays of single-moded optics to generate an array of Gaussian beams on the sky. Figure 14 shows simulations of the PIXIE beams for the \hat{x} detector on the left side of the instrument (L_x ; cf Eq. 2.1). We use a Monte Carlo ray-trace code to propagate 10^{11} random rays from the detector through the full PIXIE optics to the sky. Deviations in the position or orientation of the concentrator and mirrors will affect the beam pattern. To account for such tolerance effects, each Monte Carlo realization independently perturbs each optical element in both position and orientation by an amount drawn from a Gaussian distribution whose width is set by typical machining/assembly tolerances of 0.05 mm. The dominant effect of such tolerance errors is an anti-symmetric response in the beam difference.

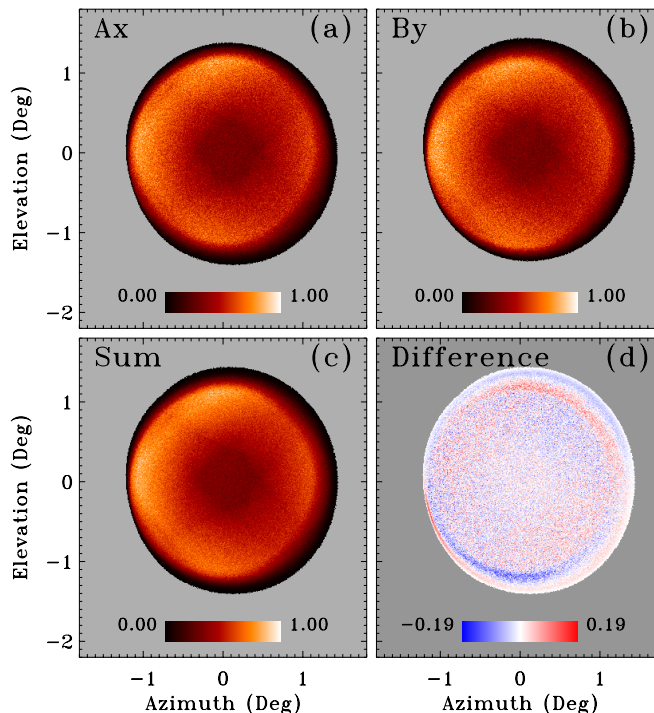


Figure 14. Monte Carlo realization of the beam patterns for the P_{L_x} detector, generated from a ray trace of 10^{11} rays from the detector through the optics to the sky. (a) \hat{x} polarization in the A-side beam. (b) \hat{y} polarization in the B-side beam. (c) $(A_x + B_y)/2$ sum. (d) $(A_x - B_y)/2$ difference. Plots (a) and (b) are normalized to unity at the peak. Tolerance errors in the individual optical elements create a small offset in beam position (see text).

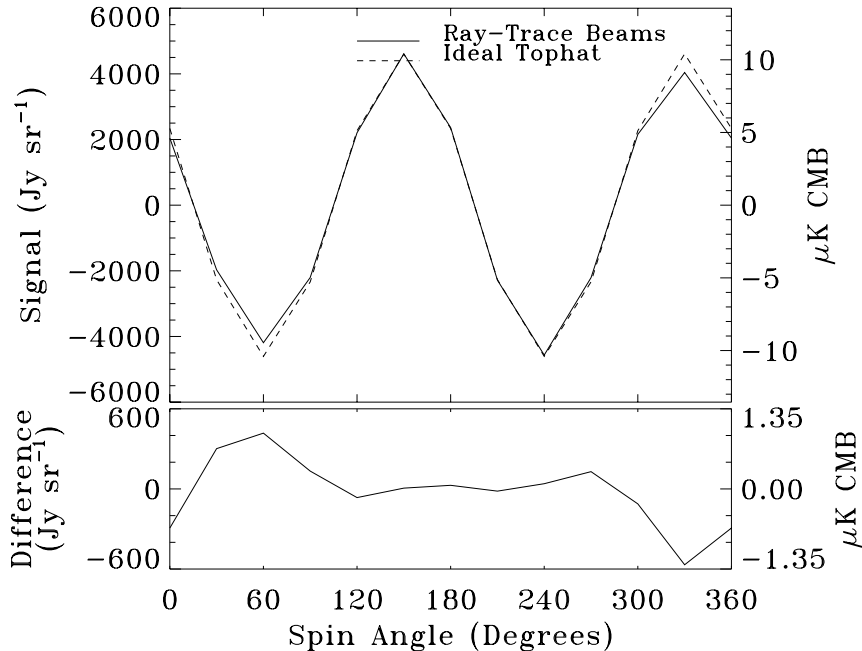


Figure 15. Comparison of the spin-modulated signal for a single PIXIE detector between ideal tophat beams and the Monte Carlo ray-trace beam patterns (Fig. 14) for a single mid-latitude pixel at 270 GHz. The difference signal is dominated by a dipole term which does not couple to polarization.

The anti-symmetric component of the A-B beam difference couples to unpolarized gradients on the sky to source systematic error. The spacecraft spin allows identification and separation of symmetric vs anti-symmetric signals. The 48-second spin period is rapid compared to the great-circle scan or annual orbital precession, allowing the data within each pixel on the sky to be decomposed into m moments of the spin angle. True sky polarization is modulated at twice the spacecraft spin frequency ($m = 2$), while any anti-symmetric contribution can only appear at odd harmonics of the spin. Figure 15 shows the resulting spin modulated response for a typical mid-latitude pixel (Galactic coordinates $[l, b] = [-120^\circ, -50^\circ]$) observed at 270 GHz. We compare the response of the ray-trace beam realization (including tolerance errors) to the response from ideal circular tophat beams of identical solid angle. Both responses show the expected $m = 2$ modulation at twice the spin frequency. The difference between the ideal and realistic beams is dominated by a dipole ($m = 1$) which does not couple to the fitted sky polarization. Additional simulations of the PIXIE beams quantify the response to beam errors. For a single detector, the beam response at $m = 2$ is suppressed by 35 dB relative to the monopole $m = 0$ power. This falls to -60 dB for the double-difference when comparing different detectors. Assuming unpolarized gradients of order $15 \mu\text{K}/\text{deg}$ from from the CMB dipole and Galactic foregrounds, the corresponding systematic response in polarization is below 10 nK for a single detector and below 0.1 nK for detector pairs [13].

Angular offsets between the beam centroids and the spacecraft spin axis will also create a spin-modulated systematic error. Each detector is sensitive to the difference between the power in orthogonal linear polarizations received from the two beams (Stokes Q in instrument coordinates). Rotation of the instrument about the beam axis rotates the instrument

coordinate system relative to the sky to allow separation of Stokes Q and U parameters on the sky,

$$\begin{aligned}
S(\nu)_{Lx} &= \frac{1}{4} [I(\nu)_A - I(\nu)_B + Q(\nu)_{\text{sky}} \cos 2\gamma + U(\nu)_{\text{sky}} \sin 2\gamma] \\
S(\nu)_{Ly} &= \frac{1}{4} [I(\nu)_A - I(\nu)_B - Q(\nu)_{\text{sky}} \cos 2\gamma - U(\nu)_{\text{sky}} \sin 2\gamma] \\
S(\nu)_{Rx} &= \frac{1}{4} [I(\nu)_B - I(\nu)_A + Q(\nu)_{\text{sky}} \cos 2\gamma + U(\nu)_{\text{sky}} \sin 2\gamma] \\
S(\nu)_{Ry} &= \frac{1}{4} [I(\nu)_B - I(\nu)_A - Q(\nu)_{\text{sky}} \cos 2\gamma - U(\nu)_{\text{sky}} \sin 2\gamma] , \tag{3.9}
\end{aligned}$$

where $S(\nu)$ is the Fourier-transformed spectrum from each detector, $I = \langle E_x^2 + E_y^2 \rangle$, $Q = \langle E_x^2 - E_y^2 \rangle$, and $U = 2\text{Re}\langle E_x E_y \rangle$ are the Stokes polarization parameters and γ is the spin angle, defined relative to meridians of ecliptic longitude. If the beam centroids are not aligned with the spacecraft spin axis, the beams trace circles on the sky centered on the spin axis. The resulting sampling of different locations on the sky will couple to spatial gradients on the sky to source a spin-dependent systematic error. Sky gradients on scales larger than the 2.65° tophat beam are dominated by the CMB dipole, sourcing gradients of typical scale $15 \mu\text{K}/\text{deg}$. Galactic and zodiacal foregrounds contribute additional gradients. Large-scale gradients combine with the spacecraft spin to create a dipolar response with respect to the spin angle (spin moment $m = 1$).

We evaluate the systematic error from fixed beam offsets using simulations. We first generate sky maps in each of the Stokes IQU parameters using a superposition of the CMB dipole, unpolarized anisotropy, and E-mode polarization, to which we add the Planck model of synchrotron and dust emission. We then use Eq. 3.9 to generate the signal on a single detector at each of 12 spin angles γ uniformly spaced from 0 to 2π . At each spin angle, we offset the A and B beams, independently convolve the IQU sky maps with the A and B beams, then combine the beam-convolved maps to produce the detected signal. We model the beams using a ray-trace realization including tolerance errors (Fig. 14).

Figure 16 shows the systematic error signal resulting from a $100''$ offset between the A and B beams observed for a typical mid-latitude sky pixel within a single synthesized frequency channel at 270 GHz. With both beams open to the sky, the true sky signal (solid line) shows the expected $m = 2$ dependence on the spin angle. Unpolarized gradients source a smaller $m = 1$ dipole (dashed line), which can be compared to the measured sky gradient to determine and correct the beam offset.

The 48-second spin period is commensurate with the 4-second mirror stroke so that a full rotation of the instrument relative to the sky encompasses 12 mirror strokes uniformly spaced in spin angle. Tagging each IFG within a pixel by the spin angle enables a Fourier decomposition in harmonics m of the spin frequency to order $m = 6$. The uniform sampling in γ within each pixel minimizes covariance between the orders m . Figure 17 shows the amplitude of the systematic error from beam offsets as a function of spin moment m (again evaluated at a single 270 GHz PIXIE channel). As with errors due to internal beam structure [13], the systematic error at the cosmologically-relevant $m = 2$ is suppressed by 35 dB relative to the dominant $m = 1$ effect. The nominal noise of 75 Jy sr^{-1} for observations of a single pixel at a single frequency channel allow determination of the beam offsets to accuracy $6''$, reducing the residual $m = 2$ error to negligible levels (0.1 nK at 270 GHz). In practice, the mapping pipeline will include 4 additional free parameters to describe the offsets of the A

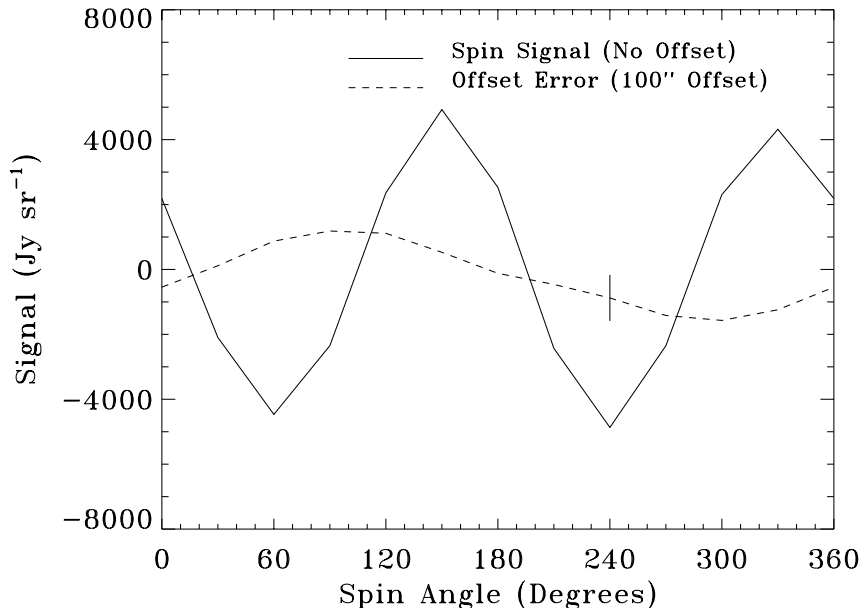


Figure 16. The systematic error signal from a beam offset of $100''$ is shown for polarized observations of a single mid-latitude pixel ($l = -120^\circ$, $b = -50^\circ$) at a single synthesized frequency of 270 GHz (the peak of the CMB $\partial B/\partial T$ anisotropy spectrum). The solid vertical bar represents the noise at each spin angle. The true sky polarization (solid line) shows the expected $m = 2$ dependence on spin angle, while the systematic error (dashed line) is dominated by a dipole ($m = 1$) response.

and B beams, using the full multi-pixel, multi-frequency data set to fit the beam centroids to few-arcsecond accuracy.

Measurements of spectral distortions are much less sensitive to beam errors. With the calibrator deployed to block one beam, information on the unpolarized intensity is contained within the $m = 0$ spin mode (Eq. 3.9). Regardless of the actual beam shape, the spin-averaged $m = 0$ beam is azimuthally symmetric. Deviations from azimuthal symmetry in the individual beam profiles couple to higher-order spin terms $m > 0$ and do not couple to spectral distortions (§4.4).

3.2.4 MTM Position Errors

The Fourier transform from the measured interferograms to the synthesized frequency spectra assumes that the phase-delay mechanism is in the correct position for each detector sample. Differences between the nominal and actual positions modulate the synthesized spectra to create both random (noise) terms and coherent systematic terms. Nagler et al. (2015) [12] discuss the simplest case of a fixed phase offset, either from a metrology error or a timing error such that the detector samples do not line up onto zero path difference (ZPD). A fixed position offset Δz in the IFG sampling produces errors in both the real and imaginary parts

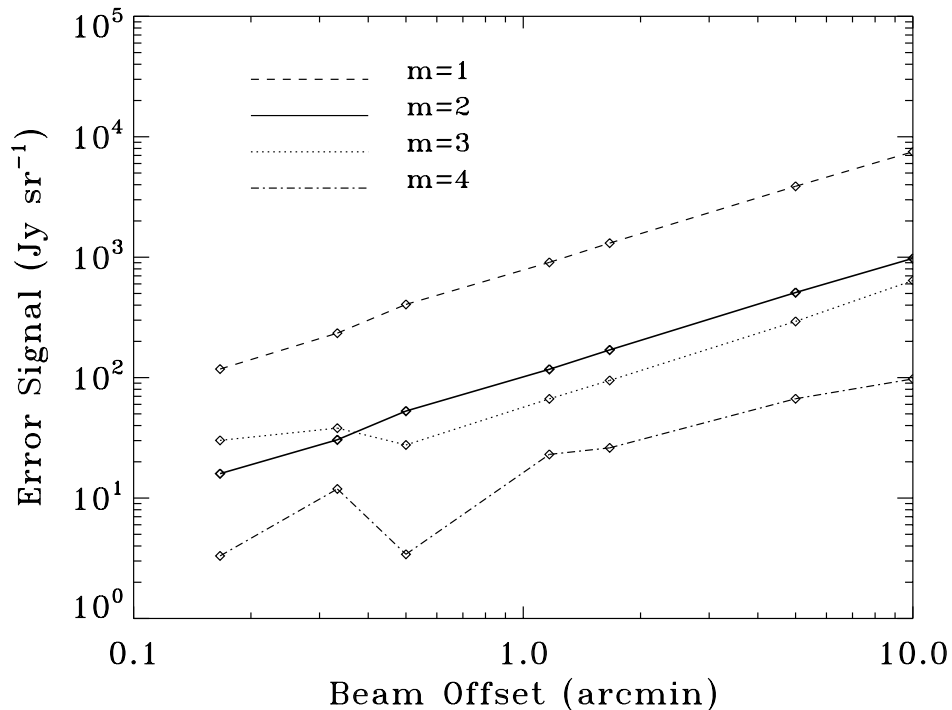


Figure 17. The amplitude of systematic errors from beam offsets depends on the distance by which the beam centroid differs from the spacecraft spin axis. The resulting differential beam patterns couple to unpolarized gradients on the sky to produce an anti-symmetric signal dominated by the $m = 1$ spin dipole.

of the synthesized spectra,

$$\begin{aligned}\Delta S_{\nu}^{\text{Re}} &= S_{\nu} (2\pi(\nu\Delta z/c)^2) \\ \Delta S_{\nu}^{\text{Im}} &= S_{\nu} (2\pi(\nu\Delta z/c)) \ ,\end{aligned}\tag{3.10}$$

modulating to the incident spectrum S_{ν} by terms proportional to powers of the position offset Δz . The effect appears at first order in Δz for the imaginary spectra and at second order for the real spectra. For position errors Δz less than the $7 \mu\text{m}$ mirror step size, the effect in the real spectrum is suppressed by 2–4 orders of magnitude relative to the imaginary spectrum over the PIXIE frequency range. ZPD errors may thus be removed by fitting a single phase term Δz to minimize the imaginary part of the Fourier transform. A single phase correction fit to the full mission data removes a single degree of freedom from over 10^7 discrete IFGs, reducing the error to levels $\delta S_{\nu}^{\text{Re}} < 10^{-6} \text{ Jy sr}^{-1}$ with negligible increase in noise.

Random errors in the mirror position produce a related effect. The interferogram amplitude at the i^{th} position sample may be represented by the cosine transform

$$P_i = \int (S(\nu) \cos(2\pi\nu/c z_i) d\nu)\tag{3.11}$$

up to normalizing constant (Eq. 2.1). For random position errors $\delta z \ll z$ we may re-write

this as

$$\begin{aligned}
P_i &= \int S(\nu) \cos(\phi_i + \delta\phi_i) d\nu \\
&= \int S(\nu) [\cos(\phi_i) \cos(\delta\phi_i) - \sin(\phi_i) \sin(\delta\phi_i)] d\nu \\
&= \int S(\nu) \left[\cos(\phi_i) \left(1 - \frac{\delta\phi_i^2}{2}\right) - \delta\phi_i \sin(\phi_i) \right] d\nu
\end{aligned} \tag{3.12}$$

where for clarity we adopt notation $\phi = 2\pi\nu/cz$. The first term is the nominal IFG amplitude reduced by a factor $1 - \delta\phi_i^2/2$. Over many IFG realizations, we may replace the individual position variance δz_i^2 with the mean $\langle \delta z_i^2 \rangle$. After Fourier transform to the frequency domain, the resulting systematic error in the synthesized spectra is proportional to $S(\nu)(1 - \langle \delta\phi_i^2 \rangle / 2)$ and may be subsumed into the overall calibration.

The second term varies as $\delta\phi_i \sin(\phi_i)$ and sums to zero over repeated iterations of the mirror stroke. Within any single IFG, it represents an effective noise term. Figure 18 compares the phase noise to the instrument white noise after Fourier transform to the frequency domain. The left panel shows the measured position errors δL for the PIXIE phase delay mechanism. Including the folding of the optical path, position error $\delta L = 20$ nm corresponds to optical error $\delta z = 80$ nm. The right panel shows the phase noise term from a single IFG realization where $z_i \rightarrow z_i + \delta z_i$ with δz_i drawn from a random Gaussian distribution of width 80 nm. The phase noise for a typical mid-latitude pixel is 2 orders of magnitude below the instrument noise for each IFG, and integrates down as \sqrt{N} for additional samples.

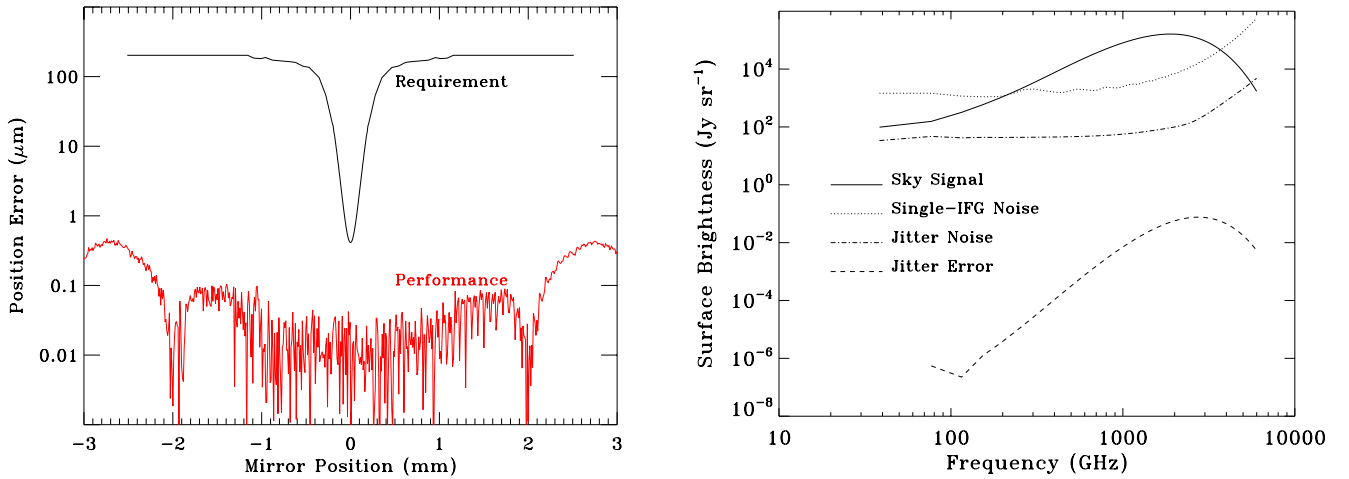


Figure 18. Effects of position error in the phase delay mechanism are small. (left) Measured position errors δL in the phase delay mechanism (red curve) are well below the mission requirements. (right) The noise term from random phase delay errors (dot-dash line) is shown for a single IFG realization with Gaussian position errors $\delta L = 20$ nm ($\delta z = 80$ nm). The phase noise is small compared to the instrument white noise, and integrates down with subsequent realizations. The lower dashed line shows the coherent systematic error. This term does not integrate down, but is subsumed into the overall calibration.

3.2.5 Spatial Interferometry

When the calibrator is stowed, the spatial separation of the two primary mirrors creates a phase difference $\tau = \vec{b} \cdot \vec{s}/c$ between the two parallel sky beams, where \vec{s} is the vector from beam center to the sky and \vec{b} is the baseline from the center of the A-side primary to the B-side primary. Including this effect, the power at each detector may be written as [12]

$$\begin{aligned}
 P_{Lx} &= \frac{1}{2} \int I + Q \cos(z\omega/c) + [V \cos(\omega\tau) - U \sin(\omega\tau)] \sin(z\omega/c) d\omega \\
 P_{Ly} &= \frac{1}{2} \int I - Q \cos(z\omega/c) + [V \cos(\omega\tau) + U \sin(\omega\tau)] \sin(z\omega/c) d\omega \\
 P_{Rx} &= \frac{1}{2} \int I + Q \cos(z\omega/c) + [-V \cos(\omega\tau) - U \sin(\omega\tau)] \sin(z\omega/c) d\omega \\
 P_{Ry} &= \frac{1}{2} \int I - Q \cos(z\omega/c) + [-V \cos(\omega\tau) + U \sin(\omega\tau)] \sin(z\omega/c) d\omega \quad (3.13)
 \end{aligned}$$

where $V = 2 \text{Im}(E_x E_y^*)$ is the Stokes parameter for circular polarization and for clarity we have suppressed the notation for the optics transmission and detector efficiency.

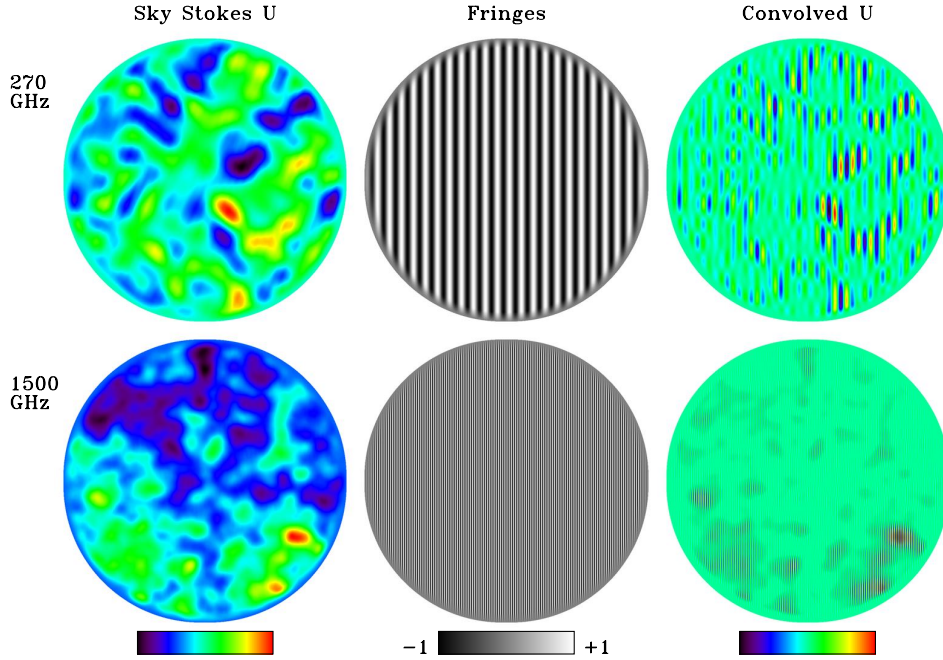


Figure 19. The spatial separation of the two sky beams sources a systematic error in the imaginary Fourier transform proportional to Stokes U . The top row shows the effect at frequency 270 GHz, while the bottom row shows the effect at 1500 GHz. (Left) Sky signal in Stokes U for a typical mid-latitude patch (Center) Fringe pattern from operation as a 2-element interferometer (Right) Sky signal convolved with the fringe pattern. The oscillatory fringe pattern across the beam leads to nearly complete cancellation of the systematic error.

Treating PIXIE as a 2-element spatial interferometer adds two additional terms in instrument-fixed coordinates: one term proportional to linear polarization (Stokes U) and a second term proportional to circular polarization (Stokes V). Both terms are modulated by $\sin(z\omega/c)$ from the mirror movement and thus appear only in the imaginary part of the Fourier transform. Several factors combine to make these “2-element-array” terms small. The millimeter sky is dominated by the CMB and diffuse dust cirrus, neither of which is thought to emit in circular polarization. Terms proportional to Stokes V can thus be neglected. The Stokes U term will be dominated by CMB E-mode polarization and diffuse foreground emission. This term must be integrated over the primary beam pattern. Since the baseline \vec{b} separating the two mirrors is normal to the antenna boresight, the phase lag $\tau = 0$ for a point source on-axis, and oscillates as

$$\sin\left(\frac{2\pi b}{\lambda}\theta\cos(\phi)\right) \quad (3.14)$$

over the beam for off-axis sources, where θ is the radial distance from beam center and the azimuthal angle ϕ is defined relative to the centerline connecting the two primary mirrors. For mirror separation $|b| = 60$ cm, the ratio $b/\lambda \gg 1$ at the accessible PIXIE wavelengths $\lambda > 2$ cm.

Figure 19 illustrates the effect of 2-beam spatial interferometry. We show the sky signal in Stokes U for a representative mid-latitude patch $[l, b] = [-120^\circ, -50^\circ]$ consisting of the CMB E-mode polarization and the Planck model of dust polarization, evaluated at frequencies 270 GHz near the CMB peak and 1500 GHz near the dust peak. The fringe pattern goes through multiple oscillations across the beam. Integrating across the beam, the fringe oscillations suppress the error term $U\sin(\omega\tau)$ by a factor of 40 (200,000) at 270 GHz (1500 GHz) relative to the incident Stokes U sky signal integrated over the beam.

4 Jackknife Tests

Jackknife tests are commonly employed by CMB missions as a blind test to characterize the noise and search for residual systematic error. Examples include differences between the first and last half of the mission, day vs night observations, or data taken with and without potential noise sources present (e.g. radio-frequency transmitters). PIXIE can employ all of these tests; however, discrete symmetries within the PIXIE instrument design and mission operations provide additional jackknife tests to detect, model, and remove potential systematic errors from the data. Table 1 lists the principal instrument symmetries and their associated jackknife tests.

4.1 Detector Pairs

Each of the four detectors samples a unique linear combination of signals from the \hat{x} polarization in one beam and the \hat{y} polarization in the other beam (Eq. 2.1). The \hat{x} detector on left side of the instrument sees the same sky signal (with a minus sign) as the \hat{y} detector on the right side, while the \hat{x} and \hat{y} detectors sharing each concentrator view the same sky signal delayed 90° in spacecraft spin. The spin-delayed x-y difference cancels sky signal to first order, allowing detector cross-calibration. Signals reverse sign upon the double interchange left-right and x - y so that the linear combinations $(P_{Lx} + P_{Ry})/2$ and $(P_{Ly} + P_{Rx})/2$ contain no sky signal (independent of spin). A non-zero signal in the $L - R$ jackknife points to differences in the detector absorption efficiency or transmission through the optics.

Table 1: Instrument Jackknife Symmetries

Symmetry	Time Scale	Test
Left/Right Detectors	4 ms	Polarization & optical efficiency
Forward/Reverse Mirror Stroke	4 sec	Time constants in full readout chain
Real/Imaginary FFT	4 sec	1/ f noise, general diagnostic
X/Y Polarization	12 sec	Detector cross-calibration
Spin ($m = 3 - 6$)	8-16 sec	Beam shape, spacecraft thermal effects
Spin ($m = 1$)	48 sec	Beam alignment
A/B Optics	5 hrs	Optical efficiency
Hot/Cold Calibrator	10 hours	Detector non-linearity
Hot/Cold Optics	10 hours	Stray Light
Spin CW/CCW	2 years	Far sidelobes
Ascending/Descending Node	6 months	Sky Gradients, spacecraft thermal effects

More generally, the four detectors have 12 possible pairwise linear combinations (Appendix A). Jackknife comparison of detector pairs tests both the polarized detector absorption efficiency ϵ as well as the transmission f through the A- and B-side optics from the detector to the sky (or calibrator). Since both ϵ and f are defined relative to the external blackbody calibrator, any differences $\epsilon_i - \epsilon_j$ or $f_A - f_B$ appear at second order in the sky data and may be identified and corrected at this level by the pairwise detector comparison (§4.5).

Differences in the beam patterns can also produce detector-specific error signals [13]. These can be distinguished from differences in detector absorption efficiency or optical transmission by their dependence on spacecraft spin (§4.4).

4.2 Mirror Stroke

The ideal interferograms on each detector depend only on the absolute value of the optical phase delay, or equivalently, the absolute mirror displacement from zero path difference. The full mirror stroke, from the far stop through zero path difference to the near stop and then back again, provides 4 copies of the sky data with different space/time symmetries (Figure 20).

Time reversal symmetry provides a straightforward evaluation of time constants in the readout chain. This includes both the thermal time constant(s) intrinsic to each detector, as well as time constants or filters employed in the post-detector readout electronics. Figure 21 shows an example. Detector time constants act as a single-pole filter, with error signal proportional to the time derivative of the incident signal

$$P_i \rightarrow P_i + \alpha P_{i-1} , \tag{4.1}$$

where P_i refers to the power at the detector for the i^{th} time-ordered sample. We first generate a set of interferograms for a full mirror stroke, using as inputs a sky model with CMB, synchrotron, dust continuum spectra plus the bright CII and CO lines, with the calibrator held 0.3 mK above the CMB. We then process the time-ordered IFG from the true sky signals through a single-pole filter with 256 Hz sampling and detector time constant 7 ms to create as-observed IFGs for the forward and reverse mirror strokes. The top panel of Figure 21 compares the resulting forward and reverse IFGs.

The delay induced by the detector time constant causes the observed IFGs to differ from the true sky signal (bottom panel of Figure 21). Sorting the IFGs by mirror direction identifies the resulting systematic error and provides a first-order correction. The (forward

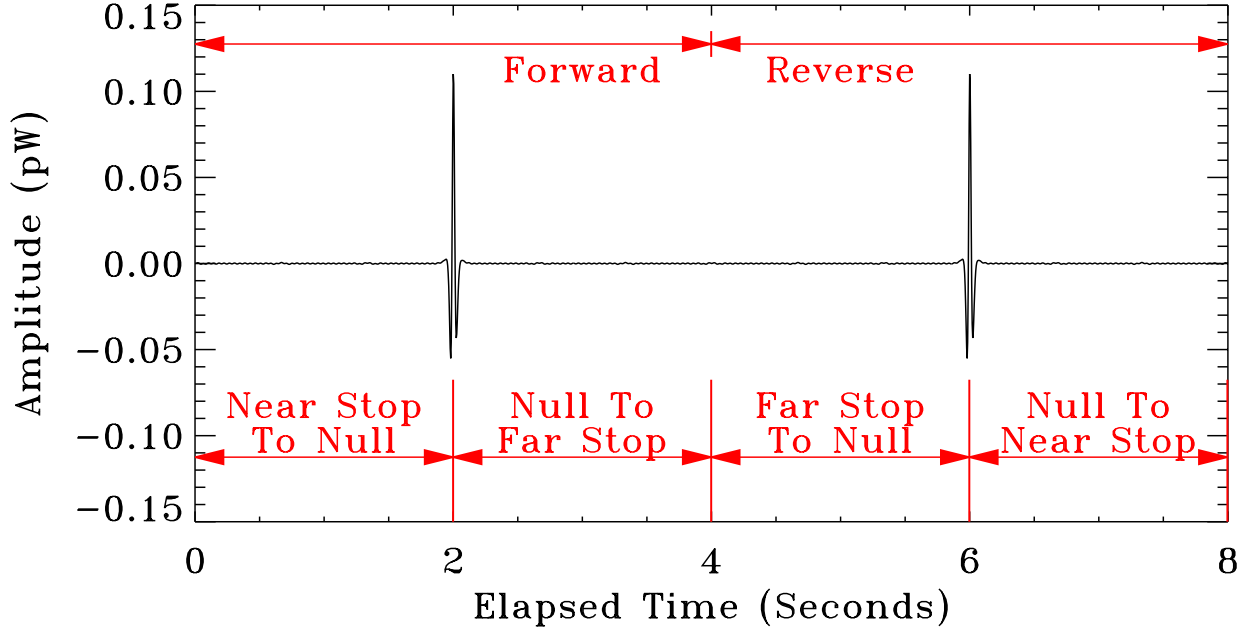


Figure 20. The phase delay mirror stroke provides 4 copies of the sky information with different spatial/temporal symmetries. Jackknife tests exploiting these symmetries correct for systematic errors resulting from the mirror zero position offset and detector time constants.

+ reverse) IFG sum is symmetric about zero path difference, and provides an initial estimate for the sky signal. The (forward-reverse) IFG difference is anti-symmetric about ZPD and provides a first-order correction. A two-year mission provides 15 million repetitions of the mirror stroke for each detector. Since the Fourier-transformed sky spectra are referred to the calibrator Planck spectrum, residual errors after correction appear at second order in the calibration and at third order in the sky spectra.

The mirror stroke also enables a determination of the mirror position at zero path difference. Physical differences in the optical path between the two sides of the instrument as well as offsets in the mirror position readout can create a systematic difference Δz between the mirror location at commanded position $z = 0$ and the actual mirror location at the white-light peak. Let

$$P_s(z) = \frac{1}{2} [P_F(z) + P_R(z)] \quad (4.2)$$

$$P_d(z) = \frac{1}{2} [P_F(z) - P_R(z)] \quad (4.3)$$

represent the symmetric sum and anti-symmetric difference of the forward and reverse mirror strokes, sorted by mirror position. Since true sky signals obey $P_s(z) = P_s(-z)$ for all mirror positions z , the jackknife $P_s(z) - P_s(-z)$ tests for fixed phase errors in z .

4.3 Real and Imaginary Fourier Transform

The Fourier transform of the sampled interferograms produces frequency spectra $I(\nu)$ with both real and imaginary terms. By symmetry, only the real part contains sky signals, while the imaginary part contains an independent realization of the noise plus systematic errors

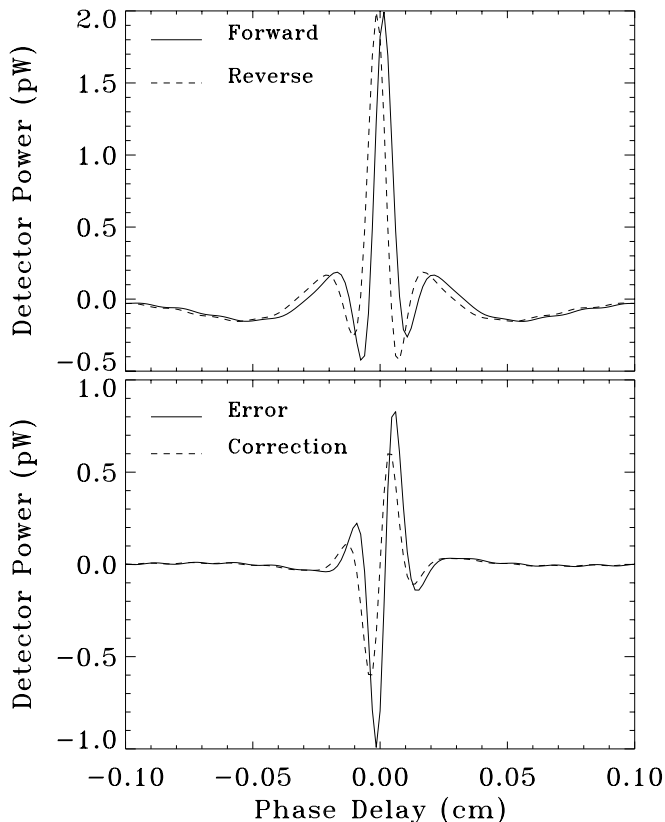


Figure 21. (Top) Interferograms from the forward and reverse mirror directions show the delay from the detector time constant. (Bottom) The anti-symmetric component of the forward/reverse mirror strokes provides a first-order correction to the error between the measured IFGs and the true sky signal.

from any effects that are not symmetric with respect to mirror position $|z|$. This includes mirror position errors from ZPD offsets (§3.2.4) as well as transient position errors excited as the mirror reverses direction at the end of each sweep. Systematic errors in mirror position resulting from the mirror turnaround are identified by comparing the IFG at start of each sweep to data at the end of the preceding sweep (when transport transients have decayed away). Although the resulting signal may be identified and modeled using the imaginary transform, in practice it is simpler to discard samples near mirror turnaround as part of the IFG apodization. Since data far from ZPD primarily encode line emission, the effect is a few-percent decrease in line sensitivity with no significant effect on continuum spectra.

All data products produced from the real Fourier transform (sky maps, frequency spectra, power spectra, etc) can also be generated from the imaginary transform. Since both the real and imaginary Fourier outputs are generated from the *same* input data set, the resulting noise estimates in the imaginary part are present at full mission sensitivity and include all effects of sampling, calibration, and data processing.

4.4 Spin

Sorting the observations within each pixel by spacecraft spin angle allows identification and subtraction of additional systematic errors.

4.4.1 Spin Moments

The spin-independent $m = 0$ mode contains the unpolarized sky spectra (Stokes I). Regardless of the individual beam shapes, the $m = 0$ response is azimuthally symmetric (although it may contain radial information) [13].

Angular offsets between the A and B beams on the sky couple to spatial gradients on the sky to create a dipolar $m = 1$ response (§3.2.3). Data taken with the calibrator deployed to block the A beam determine the offset of the B (sky) beam, and conversely for data with the calibrator blocking the B beam. With the calibrator stowed, both beams are open to the sky to allow independent determination of the beam offsets.

The $m = 2$ term contains the sky polarization signal as well as temperature-polarization systematic error coupling from beam ellipticity. Common-mode ellipticity cancels in the A - B optical differencing, leaving only the differential A - B ellipticity. The mirror symmetry (Figure 3) minimizes the differential ellipticity. After accounting for machining and assembly tolerances, the differential ellipticity is below 3×10^{-3} for individual detectors. Linear combinations of detectors can be analyzed with respect to spin angle to further probe the differential beam patterns [13].

Higher order spin terms do not couple to either intensity or polarization. The measured response can be compared to predictions based on beam models as a blind test for the beam shape. Thermal or electrical effects (either additive or multiplicative) sourced by the three-fold symmetry of the solar panels occur at $m = 3$.

4.4.2 Clockwise vs Counterclockwise

Azimuthal structure in the far sidelobes couples to gradients in the sky (primarily of Galactic origin) to source signal variation at $m = 1$. The spacecraft spin about the beam axis reverses each year, with one year in clockwise rotation followed by a second year in counterclockwise rotation. Reversing the spin direction reverses the time-ordered $m = 1$ signal while preserving the desired $m = 0$ and $m = 2$ signals. Signals sourced by solar heating of the spacecraft are likely to have a thermal phase lag with respect to the solar angle. Reversing the spacecraft spin reverses the phase lag.

4.5 A vs B Optics

Signals entering through the A and B optics appear with opposite signs on each detector (Eq. 2.1). Data taken with the calibrator covering the A beam vs the B beam provide in-flight measurement of the transmission through the optics. We sort the data from each sky pixel and sum the data taken with the calibrator blocking the A beam with those from the same sky pixel but with the calibrator blocking the B beam. We thus have

$$\begin{aligned} \Delta_{\text{cal}} &= P_{Lx}(\text{Cal}, A) + P_{Lx}(\text{Cal}, B) \\ &\propto \epsilon_{Lx} [f_A E_{x,\text{cal}}^2 - f_B E_{y,\text{sky}}^2] + \epsilon_{Lx} [f_A E_{x,\text{sky}}^2 - f_B E_{y,\text{cal}}^2] \end{aligned} \quad (4.4)$$

for the single left \hat{x} detector, with similar expressions for the other detectors. Performing the Fourier transform to derive the frequency spectra, we may write

$$\begin{aligned} \Delta_{\text{cal}}(T_A, T_B) &= \epsilon_{Lx} [M(B_\nu(T_A) - B_\nu(T_B)) + D(B_\nu(T_A) + B_\nu(T_B)) \\ &\quad + M \mathbf{Q}_{\text{sky}}(\nu) - D \mathbf{I}_{\text{sky}}(\nu)] \end{aligned} \quad (4.5)$$

where T_A and T_B are the calibrator temperature when deployed over the A and B beams³, $M = (f_A + f_B)/2$ is the mean transmission, $D = (f_A - f_B)/2$ is the difference in transmission between the A- and B-side optics, $\mathbf{I}(\nu) = E_x^2 + E_y^2$ is the sky intensity (Stokes I) and $\mathbf{Q}(\nu) = E_x^2 - E_y^2$ is the sky polarization (Stokes Q). We then evaluate the double difference comparing data when the calibrator over side A is held at a fixed temperature offset ΔT warmer than when over side B, to the equivalent data (on the same sky pixel) when the calibrator over side B is held at the same fixed ΔT warmer than side A,

$$\begin{aligned}\Delta_{\text{cal}}^{(1)}(\Delta T) &= \Delta_{\text{cal}}(T + \Delta T, T) - \Delta_{\text{cal}}(T, T + \Delta T) \\ &= 2M \frac{\partial B}{\partial T} \Delta T.\end{aligned}\tag{4.6}$$

The sky signals cancel, as does the term proportional to the mean calibrator power times the differential transmission, allowing a clean determination of the mean transmission through the optics. This provides the fundamental calibration to convert the digitized telemetry signals to physical units (e.g. Jy sr⁻¹)[10]. Similarly, we may hold the calibrator at the same temperature $T_A = T_B$ over both beams, and evaluate the double difference when the common temperature is increased by ΔT ,

$$\begin{aligned}\Delta_{\text{cal}}^{(2)}(\Delta T) &= \Delta_{\text{cal}}(T, T) - \Delta_{\text{cal}}(T + \Delta T, T + \Delta T) \\ &= 2D \left(B_\nu(T) + \frac{\partial B}{\partial T} \Delta T \right).\end{aligned}\tag{4.7}$$

This provides a clean determination of the differential transmission through the optics, independently for each of the 4 detectors. When combined with the pairwise detector jackknife tests (Appendix A), both the optics transmission f and the detector absorption efficiency ϵ can be measured and tracked throughout the flight.

4.6 Hot vs Cold Calibrator

Data with the calibrator deployed provide in-flight measurements of the detector non-linearity. The loading on an individual detector is dominated by the CMB monopole. Changes in the loading from the sky signal variation are dominated by the 3 mK CMB dipole, which changes the mean loading by 0.25%. At the start of each great-circle scan, the calibrator is moved to a new position and set to a new temperature. The temperature setpoints span the range [2.720, 2.730] K to bracket the CMB monopole at 2.725 K. Calibration thus varies the detector loading by $\pm 0.7\%$ so that the detector performance is always interpolated between values measured in flight. Calibrator temperature excursions of ± 5 mK from a single great-circle comparison provide a signal-to-noise ratio above 10^3 within individual frequency channels, allowing any changes in detector performance to be monitored throughout flight[10].

4.7 Hot vs Cold Optics

Losses in the optics terminate within the instrument and are replaced by photons emitted at the instrument temperature. Each of the surfaces within the instrument is individually controlled in temperature. The set of temperature setpoints is updated twice per great-circle scan to provide a unique temperature profile vs time for each surface (§3.1.2), which can be compared to the detector total power to determine the effective optical coupling from the

³By definition, a blackbody is unpolarized so that $E_{x,\text{cal}}^2 = E_{y,\text{cal}}^2$.

detector to each surface. Stray-light signals that pass through the mirror phase delay change sign when the surface is warmer vs colder than the sky/calibrator temperature, allowing a second measure of their coupling through corresponding changes in the interferograms.

4.8 Ascending vs Descending Node

The spacecraft scans the beams through a great circle in ecliptic coordinates, perpendicular to the sun line. As the beams move across the sky, hot and cold spots on scales much smaller than the beams enter and exit the field of view, creating a source of signal variation on time scales comparable to or shorter than the mirror stroke. Signal variation on short time scales correspond to high spatial frequencies and are Fourier transformed into a noise term at THz frequencies [14]. Since the signal variation is not symmetric with respect to the mirror stroke, noise models derived from the imaginary part of the Fourier transform (§4.3) include this term.

Every six months, the beams retrace the same great circle on the sky but in the opposite direction, reversing the time sequence from small-scale anisotropy entering and exiting the beams. Differencing the interferograms from the ascending vs descending node observations within each pixel provide a second way to isolate and quantify the noise contribution from small-scale anisotropy.

5 Discussion

Minimization, identification, and correction for potential systematic errors play a critical role for precision measurements of CMB spectral distortions or polarization. In many respects PIXIE represents a modernized version of the seminal FIRAS instrument, whose measurements of the CMB spectrum are still unsurpassed some 30 years later. PIXIE improves the FIRAS design in several significant ways. PIXIE’s colder detector temperature (0.1 K vs 1.4 K) allows operation near the limit imposed by photon statistics, while the larger etendue ($4 \text{ cm}^2 \text{ sr}$ vs $1.5 \text{ cm}^2 \text{ sr}$ per detector) allows more photons to be detected. The FIRAS measurements were not limited by systematic effects, but by the instrument noise during the limited integration time spent observing the external calibrator through the single sky horn [17]. PIXIE’s 2-beam design allows the sky and external calibrator to be observed simultaneously, ensuring equal integration time for both sky and calibrator. Additional design modifications provide the necessary control of systematic effects to take advantage of the improved sensitivity. FIRAS maintained the sky horn and calibrator at 2.725 K but held the FTS and detectors at temperature 1.4 K, 1.3 K below the CMB or external calibrator. PIXIE closely approximates a blackbody cavity, with all optical components except the detectors maintained within 5 mK of the CMB temperature. FIRAS interfered a single sky beam against an internal calibrator, while PIXIE’s fully symmetric design interferes two sky beams including all instrument optical elements. The differential optics provide pre-detection cancellation of potential systematic errors while enabling a number of jackknife tests to identify, model, and correct residual errors.

Figure 22 summarizes the systematic error budget for measurements of CMB spectral distortions. The two largest effects, cosmic ray hits and position jitter in the phase-delay mechanism, create additional noise terms at levels 10 to 100 times below the instrument noise, but do not inject coherent spectral signals. Since these are noise terms, they integrate down with observing time and are shown in Fig 22 for the nominal two-year mission. The largest spectral signature, from assumed 1% differential emissivity within the beam-forming

optics (§3.1.2), is two orders of magnitude below the instrument noise and three orders of magnitude below the cosmological μ distortion. All other effects are smaller still. We normalize the amplitude for additive (post-detection) signals by scaling the results of §3.1.1, using sinusoidal signals with amplitude equal to 10% of the instrument noise integrated over a single spacecraft spin period (so as to avoid detection in a single spin). We normalize the amplitude of spin-modulated gain variation at $\delta G/G = 10^{-4}$, set by the upper limit of 10 mK thermal variation of the instrument electronics at the spacecraft spin period (§3.2.1). Both effects contribute negligibly to the systematic error budget.

Figure 23 summarizes the systematic error budget for B-mode polarization. We use both the spectral and spatial distribution of each systematic error signal to quantify the expected contribution of each source to B-mode polarization in the CMB. For each error term, we first simulate time-ordered data to generate the Stokes IQU parameters in each spatial pixel and each frequency channel for the full two-year mission. We then fit the frequency spectra within each pixel to the CMB $\partial B/\partial T$ anisotropy spectrum to derive the amplitude of the component mimicking CMB anisotropy in each Stokes component. Finally, we use the HEALPIX `anafast` code to derive the B-mode power spectrum from the resulting Stokes Q and U maps in the fitted CMB component at Galactic latitudes $|b| > 20^\circ$. The largest term ($1/f$ noise with knee frequency 0.1 Hz) is an order of magnitude below the white noise contribution, but does not contribute coherent structure to the power spectrum. The next largest term is the residual error from beam offsets after fitting the 2-year mission for the individual offsets in the A and B beams for each detector (§3.2.3). An additive sine wave

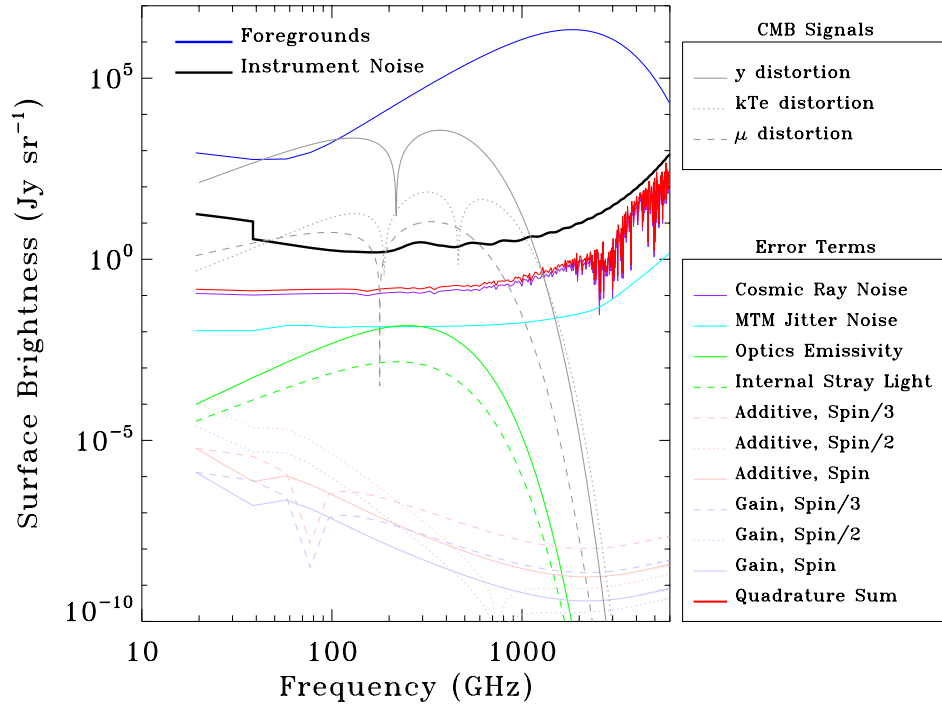


Figure 22. PIXIE systematic error budget for spectral distortions. Individual curves show the residual systematic error terms, after correction, and the quadrature sum. The combined systematic errors are small compared to cosmological signals or the baseline 2-year mission noise.

with amplitude 10% of the white-noise level at twice the spin frequency lies over 6 orders of magnitude below the noise. Systematic errors from gain variations $\delta G/G = 10^{-4}$ at twice the spin frequency are smaller still. All systematic error terms have white-noise angular power spectra (C_ℓ independent of ℓ) which further distinguishes them from the inflationary B-mode signal on large angular scales.

It is important to note that PIXIE’s systematic error suppression does not rely on any single cancellation to achieve the mission goals, but instead chains together multiple symmetries to successively reduce potential errors. PIXIE closely approximates a blackbody cavity, maintaining the calibrator, optics, and absorbing walls within a few mK of the CMB sky temperature. The largest possible instrumental spectral signature is thus of order a few mK, which is reduced to tens of μK by typical percent-level mirror emissivity. Any spectral signatures generated on one side of the instrument are then differenced against comparable signals from the other side. Percent-level differences in the optical symmetry then leave residuals at the few-hundred nK level. Active control of the optics temperatures periodically reverses the sign of any residual spectral signature. The weighting of hot-vs-cold observations can be adjusted in post-flight analysis to match at percent levels or better, reducing the instrumental signal to nK levels or below. A similar chain suppresses instrumental signals in polarization. The Fourier transform maps additive signals with periods longer than the mirror stroke onto the lowest synthesized frequency channels, effectively isolating such signals from the amplitude-modulated response to true sky signals. The multi-moded optics illuminate a single spatial pixel on the beam axis, producing a tophat beam with ellipticity 7%. Sky signals

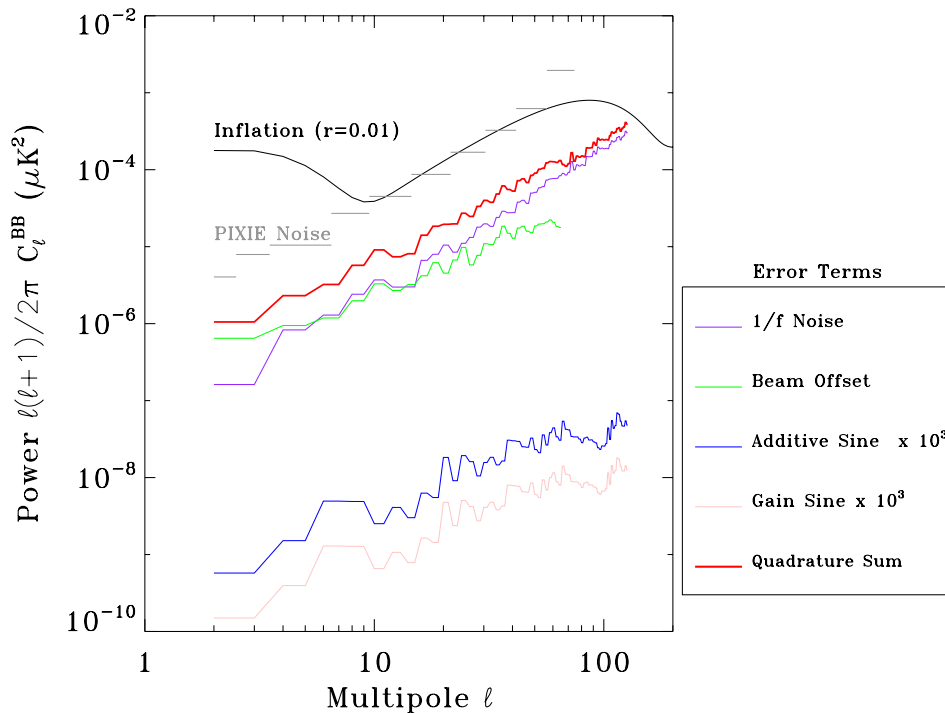


Figure 23. PIXIE systematic error budget for B-mode polarization. Individual curves show the residual systematic error terms, after correction, and the quadrature sum. The combined systematic errors are small compared to cosmological signals or the baseline 2-year mission noise.

from the two beams are differenced optically so that only the differential ellipticity couples to large-scale gradients on the sky. The left-right instrument symmetry matches the $\hat{x} - \hat{y}$ polarization difference to few-percent accuracy, reducing temperature-polarization coupling by a comparable amount. Each concentrator contains two independent detectors sensitive to orthogonal polarization states, which view the same sky pixel through the same optics. The differential ellipticity thus cancels to second order in the sum or difference comparison of different detectors. The spacecraft provides uniform sampling of the sky signal vs spin angle for each pixel over the full 2π range, cleanly separating the $m = 2$ sky polarization from the dominant $m = 1$ beam effects. The mirror stroke and spacecraft spin are fast compared to the great-circle scan motion of the beams across the sky, so that the polarization state is determined independently in each pixel, eliminating pixel-pixel covariance on angular scales larger than the beam.

6 Conclusions

We use detailed time-ordered simulations to evaluate the amplitude of systematic error signals in the PIXIE data. PIXIE combines multiple levels of null operation, signal modulation, and differencing to reduce systematic errors to negligible levels. Jackknife tests based on discrete instrument symmetries provide an independent means to identify, model, and remove remaining instrumental signals. The Fourier transform spectrometer modulates the sky signal over time scales 4 ms to 4 s. Signal drifts or post-detection pickup on longer time scales are mapped to the lowest synthesized frequency channels and do not project to the frequency or spatial distribution of either the CMB or astrophysical foregrounds. The largest systematic error signals, after identification and correction, are the residual noise terms from cosmic-ray hits to the detector absorber and the $1/f$ response of the electronics. Both appear in the spectral and polarization data as effective white-noise terms at levels of a few percent of the dominant photon noise contribution. Coherent instrumental effects, which do not integrate down with observing time, are smaller still. The largest effect for spectral distortions is the differential emissivity of the beam-forming optics. Percent-level matching of the optical properties leaves a residual systematic error with amplitude 0.1% of the cosmological μ -distortion from Silk damping of primordial density perturbations. Other effects in the frequency spectra are smaller still. Systematic errors for CMB polarization are suppressed in both the spectral and spatial dimensions. As with spectral distortions, the largest effect is the contribution from instrumental $1/f$ noise, which appears in the polarization maps as a white-noise term with amplitude one percent of the photon noise. The largest coherent effect for polarization is temperature-polarization coupling induced by offsets between the spacecraft spin axis and the individual beam boresights. The spacecraft spin allows identification and correction for beam offsets; the residual after correction has amplitude below 1% of the integrated instrument noise. Systematic errors in polarization have a white noise power spectrum (C_ℓ independent of ℓ) and are readily distinguished from cosmological signals on large angular scales.

A Pairwise Detector Comparison

The 4 detectors provide 12 distinct pairwise linear combinations. Expanding Eq. 2.1, we have

$$P_{Lx} + P_{Ly} = (\epsilon_{Lx} - \epsilon_{Ly})M\mathbf{Q} + (\epsilon_{Lx} + \epsilon_{Ly})D\mathbf{I} \quad (\text{A.1})$$

$$P_{Lx} - P_{Ly} = (\epsilon_{Lx} + \epsilon_{Ly})M\mathbf{Q} + (\epsilon_{Lx} - \epsilon_{Ly})D\mathbf{I} \quad (\text{A.2})$$

$$P_{Lx} + P_{Rx} = (\epsilon_{Lx} - \epsilon_{Rx})M\mathbf{Q} + (\epsilon_{Lx} + \epsilon_{Rx})D\mathbf{I} \quad (\text{A.3})$$

$$P_{Lx} - P_{Rx} = (\epsilon_{Lx} + \epsilon_{Rx})M\mathbf{Q} + (\epsilon_{Lx} - \epsilon_{Rx})D\mathbf{I} \quad (\text{A.4})$$

$$P_{Lx} + P_{Ry} = (\epsilon_{Lx} - \epsilon_{Ry})M\mathbf{Q} + (\epsilon_{Lx} + \epsilon_{Ry})D\mathbf{I} \quad (\text{A.5})$$

$$P_{Lx} - P_{Ry} = (\epsilon_{Lx} + \epsilon_{Ry})M\mathbf{Q} + (\epsilon_{Lx} - \epsilon_{Ry})D\mathbf{I} \quad (\text{A.6})$$

$$P_{Ly} + P_{Rx} = (\epsilon_{Rx} - \epsilon_{Ly})M\mathbf{Q} - (\epsilon_{Rx} + \epsilon_{Ly})D\mathbf{I} \quad (\text{A.7})$$

$$P_{Ly} - P_{Rx} = -(\epsilon_{Rx} + \epsilon_{Ly})M\mathbf{Q} + (\epsilon_{Rx} - \epsilon_{Ly})D\mathbf{I} \quad (\text{A.8})$$

$$P_{Ly} + P_{Ry} = -(\epsilon_{Ly} + \epsilon_{Ry})M\mathbf{Q} + (\epsilon_{Ly} - \epsilon_{Ry})D\mathbf{I} \quad (\text{A.9})$$

$$P_{Ly} - P_{Ry} = (\epsilon_{Ry} - \epsilon_{Ly})M\mathbf{Q} + (\epsilon_{Ly} + \epsilon_{Ry})D\mathbf{I} \quad (\text{A.10})$$

$$P_{Rx} + P_{Ry} = (\epsilon_{Rx} - \epsilon_{Ry})M\mathbf{Q} - (\epsilon_{Rx} + \epsilon_{Ry})D\mathbf{I} \quad (\text{A.11})$$

$$P_{Rx} - P_{Ry} = (\epsilon_{Rx} + \epsilon_{Ry})M\mathbf{Q} - (\epsilon_{Rx} - \epsilon_{Ry})D\mathbf{I} \quad (\text{A.12})$$

where $M = (f_A + f_B)/2$ is the mean transmission, $D = (f_A - f_B)/2$ is the difference in transmission between the A- and B-side optics, $\mathbf{I} = E_x^2 + E_y^2$ is the intensity (Stokes I) and $\mathbf{Q} = E_x^2 - E_y^2$ is the polarization (Stokes Q). Both the polarized detector absorption efficiency ϵ and the transmission efficiency f from the detector to the sky are expected to be slowly-varying functions of frequency.

References

- [1] A. Kogut, M.H. Abitbol, J. Chluba, J. Delabrouille, D. Fixsen, J.C. Hill et al., *CMB Spectral Distortions: Status and Prospects*, in *Bulletin of the American Astronomical Society*, vol. 51, p. 113, Sept., 2019, DOI [1907.13195].
- [2] J. Chluba, M.H. Abitbol, N. Aghanim, Y. Ali-Haïmoud, M. Alvarez, K. Basu et al., *New horizons in cosmology with spectral distortions of the cosmic microwave background*, *Experimental Astronomy* **51** (2021) 1515 [1909.01593].
- [3] G. Hinshaw, D. Larson, E. Komatsu, D.N. Spergel, C.L. Bennett, J. Dunkley et al., *Nine-year Wilkinson Microwave Anisotropy Probe (WMAP) Observations: Cosmological Parameter Results*, *The Astrophysical Journal Supplement Series* **208** (2013) 19 [1212.5226].
- [4] Planck Collaboration, N. Aghanim, Y. Akrami, M. Ashdown, J. Aumont, C. Baccigalupi et al., *Planck 2018 results. VI. Cosmological parameters*, *Astronomy and Astrophysics* **641** (2020) A6 [1807.06209].
- [5] K. Abazajian and CMB-S4 Collaboration, *CMB-S4 Science Case, Reference Design, and Project Plan*, *arXiv e-prints* (2019) arXiv:1907.04473 [1907.04473].
- [6] M. Hazumi and LiteBIRD collaboration, *LiteBIRD satellite: JAXA's new strategic L-class mission for all-sky surveys of cosmic microwave background polarization*, in *Society of Photo-Optical Instrumentation Engineers (SPIE) Conference Series*, vol. 11443 of *Society of Photo-Optical Instrumentation Engineers (SPIE) Conference Series*, p. 114432F, Dec., 2020, DOI [2101.12449].
- [7] S. Hanany and PICO Collaboration, *PICO: Probe of Inflation and Cosmic Origins*, *arXiv e-prints* (2019) arXiv:1902.10541 [1902.10541].
- [8] C.L. Bennett, A.J. Banday, K.M. Gorski, G. Hinshaw, P. Jackson, P. Keegstra et al., *Four-Year COBE DMR Cosmic Microwave Background Observations: Maps and Basic Results*, *The Astrophysical Journal Letters* **464** (1996) L1 [astro-ph/9601067].
- [9] A. Kogut, D.J. Fixsen, D.T. Chuss, J. Dotson, E. Dwek, M. Halpern et al., *The Primordial Inflation Explorer (PIXIE): a nulling polarimeter for cosmic microwave background observations*, *Journal of Cosmology and Astroparticle Physics* **7** (2011) 25 [1105.2044].
- [10] A. Kogut and D.J. Fixsen, *Calibration method and uncertainty for the primordial inflation explorer (PIXIE)*, *Journal of Cosmology and Astroparticle Physics* **2020** (2020) 041 [2002.00976].
- [11] PIXIE collaboration, *The Primordial Inflation Explorer (PIXIE): science and mission design*, *Journal of Astronomical Telescopes, Instruments, and Systems* (2023) [in preparation].
- [12] P.C. Nagler, D.J. Fixsen, A. Kogut and G.S. Tucker, *Systematic Effects in Polarizing Fourier Transform Spectrometers for Cosmic Microwave Background Observations*, *The Astrophysical Journal Supplement Series* **221** (2015) 21 [1510.08089].
- [13] A.J. Kogut and D.J. Fixsen, *Systematic error cancellation for a four-port interferometric polarimeter*, *Journal of Astronomical Telescopes, Instruments, and Systems* **5** (2019) 024008 [1908.00558].
- [14] S.K. Næss, J. Dunkley, A. Kogut and D.J. Fixsen, *Time-ordered data simulation and map-making for the PIXIE Fourier transform spectrometer*, *Journal of Cosmology and Astroparticle Physics* **2019** (2019) 019 [1710.06761].
- [15] K.M. Górski, E. Hivon, A.J. Banday, B.D. Wandelt, F.K. Hansen, M. Reinecke et al., *HEALPix: A Framework for High-Resolution Discretization and Fast Analysis of Data Distributed on the Sphere*, *The Astrophysical Journal* **622** (2005) 759 [astro-ph/0409513].

- [16] A. Kogut, G.F. Smoot, C.L. Bennett, E.L. Wright, J. Aymon, G. de Amici et al., *COBE Differential Microwave Radiometers: Preliminary Systematic Error Analysis*, *The Astrophysical Journal* **401** (1992) 1.
- [17] D.J. Fixsen, E.S. Cheng, D.A. Cottingham, J. Eplee, R. E., T. Hewagama, R.B. Isaacman et al., *Calibration of the COBE FIRAS Instrument*, *The Astrophysical Journal* **420** (1994) 457.
- [18] J. Kaplan and J. Delabrouille, *Some sources of systematic errors on CMB polarized measurements with bolometers*, in *Astrophysical Polarized Backgrounds*, S. Cecchini, S. Cortiglioni, R. Sault and C. Sbarra, eds., vol. 609 of *American Institute of Physics Conference Series*, pp. 209–214, Mar., 2002, DOI [[astro-ph/0112488](#)].
- [19] W. Hu, M.M. Hedman and M. Zaldarriaga, *Benchmark parameters for CMB polarization experiments*, *Physical Review D* **67** (2003) 043004 [[astro-ph/0210096](#)].
- [20] E.F. Bunn, *Systematic errors in cosmic microwave background interferometry*, *Physical Review D* **75** (2007) 083517 [[astro-ph/0607312](#)].
- [21] M. Shimon, B. Keating, N. Ponthieu and E. Hivon, *CMB polarization systematics due to beam asymmetry: Impact on inflationary science*, *Physical Review D* **77** (2008) 083003 [[0709.1513](#)].
- [22] J. Singal, D.J. Fixsen, A. Kogut, S. Levin, M. Limon, P. Lubin et al., *The ARCADE 2 Instrument*, *The Astrophysical Journal* **730** (2011) 138 [[0901.0546](#)].
- [23] Planck Collaboration, P.A.R. Ade, J. Aumont, C. Baccigalupi, A.J. Banday, R.B. Barreiro et al., *Planck 2015 results. III. LFI systematic uncertainties*, *Astronomy and Astrophysics* **594** (2016) A3 [[1507.08853](#)].
- [24] Planck Collaboration, N. Aghanim, M. Ashdown, J. Aumont, C. Baccigalupi, M. Ballardini et al., *Planck intermediate results. XLVI. Reduction of large-scale systematic effects in HFI polarization maps and estimation of the reionization optical depth*, *Astronomy and Astrophysics* **596** (2016) A107 [[1605.02985](#)].
- [25] J.J. Bock, A.E. Lange, M.K. Parikh and M.L. Fischer, *Emissivity measurements of reflective surfaces at near-millimeter wavelengths*, *Applied Optics* **34** (1995) 4812.
- [26] C.A. Kilbourne, J.S. Adams, R.P. Brekosky, J.A. Chervenak, M.P. Chiao, M.E. Eckart et al., *Design, implementation, and performance of the Astro-H SXS calorimeter array and anticoincidence detector*, *Journal of Astronomical Telescopes, Instruments, and Systems* **4** (2018) 011214.
- [27] Planck Collaboration, P.A.R. Ade, N. Aghanim, C. Armitage-Caplan, M. Arnaud, M. Ashdown et al., *Planck 2013 results. X. HFI energetic particle effects: characterization, removal, and simulation*, *Astronomy and Astrophysics* **571** (2014) A10 [[1303.5071](#)].
- [28] Planck Collaboration, R. Adam, P.A.R. Ade, N. Aghanim, M. Arnaud, M. Ashdown et al., *Planck 2015 results. VIII. High Frequency Instrument data processing: Calibration and maps*, *Astronomy and Astrophysics* **594** (2016) A8 [[1502.01587](#)].
- [29] Planck Collaboration, N. Aghanim, Y. Akrami, M. Ashdown, J. Aumont, C. Baccigalupi et al., *Planck 2018 results. III. High Frequency Instrument data processing and frequency maps*, *Astronomy and Astrophysics* **641** (2020) A3 [[1807.06207](#)].
- [30] T.L. Svalheim, K.J. Andersen, R. Aurlen, R. Banerji, M. Bersanelli, S. Bertocco et al., *BeyondPlanck X. Bandpass and beam leakage corrections*, *arXiv e-prints* (2022) arXiv:2201.03417 [[2201.03417](#)].
- [31] D. O’Dea, A. Challinor and B.R. Johnson, *Systematic errors in cosmic microwave background polarization measurements*, *Monthly Notices of the Royal Astronomical Society* **376** (2007) 1767 [[astro-ph/0610361](#)].

- [32] C. Rosset, V.B. Yurchenko, J. Delabrouille, J. Kaplan, Y. Giraud-Héraud, J.-M. Lamarre et al., *Beam mismatch effects in cosmic microwave background polarization measurements*, *Astronomy and Astrophysics* **464** (2007) 405 [[astro-ph/0410544](#)].